Geophysical Journal International

Geophys. J. Int. (2021) **0,** 1–0
GJI Seismology

https://doi.org/10.1093/gji/ggab470

Using a dynamic earthquake simulator to explore tsunami earthquake generation

Qingjun Meng [1], Benchun Duan[1] and Bin Luo [2]

[1] *Center of Tectonophysics, Department of Geology & Geophysics, Texas A&M University, College Station, TX* 77843*, United States. E-mail: qimeng@tamu.edu*
[2] *Geophysics Department, Stanford University, Stanford, CA* 94305*, United States*

Received 2021 October 18; in original form 2021 February 2

SUMMARY

Observations of historical tsunami earthquakes reveal that ruptures of these earthquakes propagate slowly at shallow depth with longer duration, depletion in high-frequency radiation and larger discrepancy of M_w–M_s than ordinary megathrust earthquakes. They can effectively generate tsunami and lead to huge damage to regional populated areas near the coast. In this study, we use a recently developed dynamic earthquake simulator to explore tsunami earthquake generation from a physics-based modelling point of view. We build a shallow-dipping subduction zone model in which locally locked, unstable patches (asperities) are distributed on a conditionally stable subduction interface at shallow depth. The dynamic earthquake simulator captures both quasi-static and dynamic processes of earthquake cycles. We find that earthquakes can nucleate on these asperities and propagate into the surrounding conditionally stable zone at slow speeds, generating tsunami earthquakes. A high normal stress asperity, representing a subducted seamount, can act as an asperity in some events but as a barrier in other events over multiple earthquake cycles. Low normal stress asperities typically act as asperities in tsunami earthquakes. The degree of velocity-weakening in the conditionally stable zone, which may sustain rupture at different speeds or stop rupture, is critical for tsunami earthquake generation and affects its recurrence interval. Distributed asperities may rupture in isolated events separated by tens of years, or in a sequence of events separated by hours to days, or in one large event in a cascade fashion, demonstrating complex interactions among them. The recurrence interval on a high normal stress asperity is much larger than that on low normal stress asperities. These modelling results shed lights on the observations from historical tsunami earthquakes, including the 1994 and 2006 Java tsunami earthquakes and 2010 Mentawai tsunami earthquake.

Key words: Friction; Seismic cycle; Numerical modelling; Earthquake dynamics; Subduction zone processes.

1 INTRODUCTION

Tsunami earthquakes, as defined by Kanamori (1972), are an unusual category of interplate earthquakes along subduction interfaces that generate much larger tsunami than their surface wave magnitudes (M_s) suggest. Compared to ordinary earthquakes, tsunami earthquakes have long durations with slow rupture speeds (e.g. slower than 1.5 km s^{-1}) and source spectra depleted in short-period energy, resulting in large discrepancy between their M_w and M_s magnitudes. They occur at the shallow, near trench region of a subduction zone.

Well-studied historical tsunami earthquakes include the 1896 Sanriku (Japan) earthquake and the 1946 Aleutian islands earthquake (Kanamori 1972), the 1947 Offshore Poverty Bay (New Zealand) earthquake (Bell *et al.* 2014), the 1992 Nicaragua earthquake (Kanamori & Kikuchi 1993), the 1994 Java earthquake (Abercrombie *et al.* 2001; Bilek & Engdahl 2007), the 2006 Java earthquake (Ammon *et al.* 2006; Bilek & Engdahl 2007) and the 2010 Mentawai earthquake (Lay *et al.* 2011). By analysing seismic and tsunami data, Kanamori (1972) found that the 1896 Sanriku and 1946 Aleutian islands earthquakes (e.g. magnitudes 6.8–7.5), which are moderate sizes but generate very large tsunamis (i.e. 'tsunami earthquakes'), have a source duration on the order of 100 s, strikingly different from 'ordinary' earthquakes that have source durations on the order of 10 s. He proposed that a weak zone near the trench may be responsible for slow deformation in these two tsunami earthquakes. As the first tsunami earthquake captured by modern broadband seismic networks, the 1992 Nicaragua earthquake has

© The Author(s) 2021. Published by Oxford University Press on behalf of The Royal Astronomical Society.

M_s of 7 and M_w of 7.6, a characteristic of tsunami earthquakes in disparity between M_s and M_w, and a very long source duration of ∼100 s (Kanamori & Kikuchi 1993). At this mid-American subduction zone, the sediments are largely subducted (e.g. no well-developed accretionary prism), resulting in a relatively weak plate interface that is responsible for slow rupture propagation (Kanamori & Kikuchi 1993).

The 1994 and 2006 Java earthquakes were studied by Abercrombie *et al.* (2001) and Ammon *et al.* (2006), respectively. Bilek & Engdahl (2007) studied both earthquakes. By relocating the main shock and its aftershocks and inverting for the main shock slip distribution using long-period surface waves and broadband body waves, Abercrombie *et al.* (2001) found that the 1994 Java earthquake involved slip on a locked patch at ∼20 km depth within a largely decoupled subduction zone. The locked patch coincides with a subducting seamount identified by Masson *et al.* (1990) from bathymetric and seismic investigations of the Java trench. Abercrombie *et al.* (2001) also concluded that the 1994 Java earthquake did not include a slow, shallow component of rupture of the kind observed for the 1992 Nicaragua earthquake. Ammon *et al.* (2006) analysed Rayleigh and body waves of the 2006 Java earthquake. They found that the event had a low rupture speed of 1.0–1.5 km s^{-1} with an overall duration of ∼185 s, and occurred near the up-dip edge of the subduction interface with 5–6 pulses of moment release superimposed on a smooth rupture. They argued that the compound nature of the 2006 Java event suggests the rupture interface involves localized patches of relatively strong, unstable friction surrounded by regions of either conditional stability or low frictional strength material. They noted that localized gravity highs are found in the vicinity of the rupture zone, which seems to imply that localized patches for the pulses (e.g. subevents) may correspond to some topographic reliefs on the subducting plane. Bilek & Engdahl (2007) relocated aftershocks of the 1994 and 2006 Java earthquakes and compared to slip distributions and bathymetry. They found high slip for the 1994 event in a region of uplifted topography, which is consistent with high slip over a subducting seamount proposed by Abercrombie *et al.* (2001). For the 2006 event, they did not find concentrated high slip in a zone of uplifted topography, though the rupture zone is a region of complex bathymetry on the subducting plate. Furthermore, they noted that the 2006 event terminates in a region just west of a large segment of uplifted topography. They argued that subducted seamounts may act as both slip asperities and barriers along the Java subduction zone. We speculate that the 2006 Java event ruptured 5–6 localized patches which may correspond to low-relief topographic highs (as implied by Ammon *et al.* 2006) and terminated just west of a large subducting seamount (as pointed out by Bilek & Engdahl 2007).

Lay *et al.* (2011) studied the 2010 Mentawai tsunami earthquake using teleseismic *P*, SH and Rayleigh waves. They found that the event ruptured up-dip of the slip region of the 2007 Kepulauan earthquake, which is an ordinary megathrust event off-shore of Sumatra. The rupture has a low rupture speed of ∼1.5 km s^{-1} with depleted short-period energy, characteristics of tsunami earthquakes at the shallow, near-trench region of subduction zones. By comparing with the 1994 and 2006 Java tsunami earthquakes that ruptured up-dip of weakly coupled megathrust zones, they argue that tsunami earthquakes may occur at up-dip of both strongly and weakly coupled portions of a subduction zone. Bell *et al.* (2014) examined the lesser-known 1947 Offshore Poverty Bay (OPB) and Tolaga Bay (TB) earthquakes along the east coast of the North Island, New Zealand. They show that these two earthquakes share many characteristics with other well-known tsunami earthquakes, including low amplitude shaking, long durations and anomalously large tsunami. In particular, the source region of the two earthquakes is directly imaged by 2-D seismic reflection profiles. They found that the locations of both the 1947 OPB and TB earthquakes are consistent with the earthquakes nucleating in the regions of seamount subduction at shallow depth (<10 km).

These previous studies on the historical tsunami earthquakes provide some conceptual understanding of observed features of tsunami earthquakes. Observed features include long duration, slow rupture speed, depletion in high-frequency radiation, and relatively shallow depth. By linking these features with geological and geophysical observations of the subduction zones (e.g. subducted sediment, bathymetry, gravity or magnetic anomalies) and frictional instability consideration (e.g. stable, conditionally stable, and unstable friction behaviours), these studies suggest a conceptual model of tsunami earthquakes, that is tsunami earthquakes are associated with ruptures on locally locked unstable patches within largely conditionally stable zones on subduction interfaces at relatively shallow depths. Frictional stability regimes are typically defined in the framework of the rate- and state-dependent friction law, in particular velocity dependence of friction (Scholz 1998). Velocity-strengthening frictional behaviour is intrinsically stable. Velocity-weakening frictional behaviour is unstable when the effective normal stress applied on the friction interface is higher than a critical value, but is conditionally stable if the effective normal stress is less than the critical value. On a conditionally stable friction interface, frictional slip is stable under quasi-static loading but unstable under dynamic loading with a sufficient velocity jump.

In understanding large tsunami generation due to megathrust earthquakes, such as the 2011 Tohoku earthquake, Ma (2012), Ma & Hirakawa (2013) and Ma & Nie (2019) examine effects of dynamic failure of wedge sediments on seafloor uplift and tsunamigenesis. They find that dynamic wedge failure provides an alternative mechanism for large tsunami generation to large plate-interface slip near the trench. They also find that dynamic wedge failure can slow down rupture propagation on subduction interfaces, contributing to slow rupture speed observed in tsunami earthquakes. By linking earthquake source properties with upper-plate elastic properties based on classical self-similar source theory and *P*-wave velocity observations of subduction zones, Sallares & Ranero (2019) and Sallares *et al.* (2021) propose that depth-dependent upper-plate elastic properties may largely determine depth-varying rupture characteristics, including features associated with tsunami earthquakes. Therefore, elastic properties of off-fault materials and their response to dynamic rupture may also contribute to tsunami earthquake generation, in addition to frictional properties on the subduction interface. However, in this study we focus on examining how frictional properties may determine the features observed in historical tsunami earthquakes, as the conceptual model suggested from previous studies has not been quantitively tested. It's likely that both frictional properties on subduction zone interfaces and material properties and response off the plate interface play important roles in tsunami earthquake generation. Comparing and quantifying their roles are worthwhile efforts for the scientific community to better understand mechanisms of tsunami earthquakes and to better assess tsunami hazards along subduction zones worldwide, which are beyond the scope of this study.

To examine how well the conceptual model in terms of the subduction-interface frictional properties works and to further quantitatively explore physical controls of these properties on observed tsunami earthquake features, we resort to physics-based earthquake

generation models. Existing and widely used earthquake generation models in the community include dynamic rupture models (e.g. Andrews 1976; Day 1982; Day *et al.* 2005; Harris *et al.* 2009, 2018), earthquake cycle models without fully dynamic coseismic process such as classical earthquake simulators (e.g. Dieterich & Richards-Dinger 2010; Pollitz 2012; Sachs *et al.* 2012; Tullis *et al.* 2012; Ward 2012) and other quasi-dynamic simulators that ignore wave-mediated stress transfers (e.g. Rice 1993; Ben-Zion & Rice 1995; Rice & Ben-Zion 1996), and earthquake cycle models with fully dynamic coseismic process (e.g. Lapusta *et al.* 2000; Lapusta & Liu 2009; Noda & Lapusta 2013). Dynamic rupture models can explore spontaneous rupture propagation (and arrest) based on physical laws in continuum mechanics, failure criteria such as Coulomb failure criterion and friction laws that control the frictional evolution on the fault during rupture propagation. However, they typically do not capture the nucleation phase of an earthquake cycle. Furthermore, the initial stress condition, which is critical in spontaneous rupture propagation, has to be assumed and may not be consistent with earthquake histories on the fault. Classical earthquake simulators and other quasi-dynamic simulators do not capture spontaneous rupture propagation, which is critical in determining the final size of an earthquake rupture. Earthquake cycle models with coseismic dynamic process (e.g. dynamic earthquake simulators) would be ideal in addressing the questions raised above. However, the dynamic earthquake simulator developed by Lapusta and coworkers (Lapusta *et al.* 2000; Lapusta & Liu 2009) are limited to vertical, planar fault geometry due to the semi-analytical solution nature of the boundary integral method used in these models. Therefore, it may not be appropriate to study earthquake behaviours on shallow-dipping subduction interfaces. Recently, we developed a dynamic earthquake simulator, based on our dynamic finite element method (FEM) EQdyna, which captures both the quasi-static and dynamic processes of an earthquake cycle (Luo *et al.* 2020). As a FEM-based simulator, it can handle complex fault geometry, with shallow-dipping thrust faults as one example compared with vertical faults.

In this study, we use the EQdyna-based dynamic earthquake simulator to quantitatively test the conceptual model for tsunami earthquake generation and to explore controls of physical parameters, including a–b in the rate- and state-dependent friction law (RSF), normal stress, and distributions and properties of locally locked patches within conditionally stable zones, on tsunami earthquake features. We will first briefly introduce the dynamic earthquake simulator. Our models to be explored are motivated by the observations in the historical tsunami earthquakes reviewed above. Then we present main results from these models and discuss implications of the results. This modelling study with the state-of-art dynamic earthquake simulator improves our understanding of tsunami earthquakes from a physical and quantitative point of view. It also demonstrates the potential of the dynamic simulator in studying earthquake cycle and faulting behaviours along subduction zones that host various slip behaviours, including damaging earthquakes and tsunamis.

2 METHOD

We use a newly developed dynamic earthquake simulator (Luo *et al.* 2020) to simulate slip behaviour on a subduction interface in this study. The dynamic simulator is based on an explicit finite element method (FEM) EQdyna that is developed for dynamic rupture simulations (Duan & Oglesby 2006; Duan & Day 2008; Duan 2010; Duan 2012; Liu & Duan 2018; Luo & Duan 2018). To simulate other quasi-static processes by the dynamic solver EQdyna, including post-seismic, interseismic and nucleation phases of an earthquake cycle, the simulator utilizes an adaptive dynamic relaxation technique (Qiang 1988) and a variable time stepping scheme (Lapusta *et al.* 2000). Thus, both the dynamic and quasi-static processes of an earthquake cycle are modelled in one FEM framework. The transition between the dynamic and quasi-static processes is controlled by the maximum slip velocity $V_{\max}$ over the entire fault as an indicator (Kaneko *et al.* 2011; Luo *et al.* 2020). The quasi-static simulation is terminated and switched to the dynamic simulation when $V_{\max}$ reaches a threshold value V_{thr}. The selection of V_{thr} is based on the balance between numerical accuracy and computational efficiency. We adopted an empirical value of $V_{\text{thr}} = 0.01\ \text{m s}^{-1}$ as the threshold for the quasi-static to dynamic transition, consistent with the choice in Chen & Lapusta (2009). We applied a smaller threshold of $V_{\text{thr}} = 0.005\ \text{m s}^{-1}$ for the dynamic to quasi-static transition.

In EQdyna, various constitutive friction laws are implemented, including slip-weakening law, the rate- and state-dependent friction (RSF) law with aging law, the RSF law with slip law, and the RSF law with slip law and strong rate weakening (Luo & Duan 2018). In this study, we adopt the RSF law with aging law (Dieterich 1979), which is commonly used in exploring major features of earthquake cycles (e.g. Lapusta *et al.* 2000; Lapusta & Liu 2009; Erickson & Dunham 2014; Yu *et al.* 2018), as shown in the equations below:

$$\tau = \sigma * \left(f_0 + a\ \ln \frac{V}{V_0} + b\ \ln \frac{V_0 \theta}{L} \right), \tag{1}$$

$$\frac{\mathrm{d}\theta}{\mathrm{d}t} = 1 - \frac{V\theta}{L}, \tag{2}$$

In RSF eq. (1), the frictional strength τ is a function of effective normal stress σ, reference slip rate and friction coefficient V_0 and f_0, slip rate V, state variable θ and characteristic slip distance L. The coefficients of a and b represent the rate-dependency and the state-dependency of the frictional strength. In the aging law, the state variable θ evolves as a function of V, θ and L, as shown in eq. (2).

The dynamic relaxation technique to solve quasi-static problems with a dynamic solver involves an iterative process that may vary from a few tens to hundreds of iterations, depending on how far the initial displacement field deviates from the static solution. Therefore, the computational need is demanding. However, because of the explicit nature of the dynamic solver EQdyna, we do not solve systems of equations, which is one convenient way to make the simulator suitable for parallelization and scaling for large-scale high-performance computing. Because the simulator is FEM-based, it can handle fault geometrical complexity, with shallow-dipping geometry of subduction zone faults as one example compared with vertical faults, and material heterogeneities. We refer readers to Luo *et al.* (2020) for more details of this dynamic earthquake simulator.

3 MODELS

Previous observational studies of tsunami earthquakes have established that (1) tsunami earthquakes occur in a largely conditionally stable frictional environment at relatively shallow depths, probably due to subducted sediments on subduction interfaces and (2) locally locked, frictionally unstable patches exist on these shallow subduction interfaces, which cause earthquake nucleation and propagation. In several of the historical tsunami earthquakes, including the 1994 Java earthquake, the 1947 Offshore Poverty Bay and Tolaga Bay earthquakes, these locally locked, frictionally unstable

patches clearly correspond to subducted seamounts (Abercrombie *et al.* 2001; Bilek & Engdahl 2007; Bell *et al.* 2014). The subduction of seamounts may increase the normal stress on the interface (Scholz & Small 1997), which could lead to asperities on an otherwise decoupled, aseismically slipping shallow subduction zone. Another mechanism that may give rise to asperities within a conditionally stable zone is permeability changes of subducted sediments (Pacheco *et al.* 1993). For example, compared to low-permeability sediments such as water-saturated clays, sediments that are more permeable such as sand could move more quickly out of the stable field of frictional behaviour as they are compacted and lithified (Pacheco *et al.* 1993), which may generate locally locked patches as asperities. In this study, we build a relatively simple subduction zone model, that is a shallow-dipping, planar thrust fault on which two or three asperities (corresponding to the above two mechanisms) are surrounded by conditionally stable zones. We use our dynamic earthquake simulator to simulate slip behaviours on this fault over multiple earthquake cycles.

3.1 Geometry, boundary conditions and material properties of the 3-D thrust fault model

In this study, we work on a 3-D pure-thrust fault model with dipping angle $\phi = 30^\circ$. The thrust fault plane intersects the free surface ($Z = 0$) with the intersecting line along the X-axis on the top of the model and dips towards $Y > 0$ (Fig. 1). We set up the boundary conditions as below. The top surface of the model is the free surface. The left and right boundaries of the model ($X = X_{\min}$ and $X = X_{\max}$) are fixed along X-axis: $u_x = 0$. The footwall moves downward parallel with the fault plane, thus a loading rate of (1/2) V_{pl}= 0.5×10^{-9} m s^{-1} downward parallel to the fault plane is assigned on the bottom surface ($Z = Z_{\min}$), on the back boundary ($Y = Y_{\min}$), and on the footwall part (below the fault) of the front boundary ($Y = Y_{\max}$). The hanging wall moves upward parallel with the fault surface, hence a loading rate of $(1/2)V_{pl} = 0.5 \times 10^{-9}$ m s^{-1} upward parallel to the fault plane is assigned to the hanging-wall part (above the fault) of the front boundary ($Y = Y_{\max}$). We remark that one may assign unequal parts of V_{pl} on the footwall and hanging wall model boundaries, which will not affect the strain accumulation on the fault (and thus the fault evolution). For the FEM mesh, we largely use hexahedral elements in the model for computational efficiency. However, to conform the shallow-dipping fault geometry, we use a degeneration technique (e.g. Hughes 2000; Duan 2010, 2012; Luo & Duan 2018) to cut a hexahedral element into two wedge elements along the fault plane. This results in a relationship among the dimensions of an element around the fault: $\Delta y = \Delta x \cos\phi$ and $\Delta z = \Delta x \sin\phi$. We use the element size along the X-axis (i.e. Δx) to characterize the spatial resolution of the FEM model, and Δy and Δz are smaller than Δx for shallowly dipping thrust faults. We use $\Delta x = 200$ m in this study (thus $\Delta y = 173$ m and $\Delta z = 100$ m for the dip angle of 30°). We assume a homogenous elastic medium in the model to focus on effects of shallowly dipping fault geometry and heterogeneous friction properties. Material properties and other relevant parameters are summarized in Table 1.

3.2 Heterogeneous distributions of fault parameters and various models

Fig. 2 shows the heterogeneous distributions of the frictional parameters a, b, a–b and L and the effective normal stress on the main fault (i.e. Plane 1 in Fig. 1) in our base Model 1. Frictional instability depends on two friction parameters in RSF, L and the combined parameter (a–b). If (a–b) ≥ 0 (i.e. velocity strengthening), frictional slip is always stable. If (a–b) <0 (i.e. velocity weakening), there is a Hopf bifurcation between an unstable regime and a conditionally stable regime (Scholz 1998). In a simple spring-slide model with spring stiffness k, the bifurcation occurs at a critical value of effective normal stress $\sigma_c = kL/(-(a-b))$. Therefore, if other parameter values are same, moving (a–b) value (still negative) closer to zero can bring the frictional interface into a conditionally stable regime from an unstable one. In Model 1, we set up two asperities Z1 and Z2 on the largely conditionally stable thrust fault, with along strike dimension of 70 km and along dip of 40 km. The asperity Z1 is a 14 km by 14 km patch with a–b of –0.004 (velocity weakening, unstable), a relatively large L of 10 mm, and a relatively high effective normal stress of 50 MPa. We denote this patch as HNS asperity (high normal stress), which may represent some effects of a shallow, subducted seamount. We remark that effects of subducted seamounts could be more complex than increasing effective normal stress. The asperity Z2 has the same size and the same value –0.004 for a–b as Z1, but a smaller L of 4 mm and a lower effective normal stress of 20 MPa than Z1. We denote this patch as LNS asperity (Low Normal Stress), which may represent a permeable sediment patch (such as sand) that is subducted deeper and becomes locally locked due to compaction and lithification. Surrounding Z1 and Z2 is the conditionally stable zone with a–b of –0.002 and the same values of L and the effective normal stress as in Z2. This zone is further surrounded by a velocity-strengthening zone (frictionally stable, i.e. Plane 2 in Fig. 1) on the boundary and outside of the main fault (i.e. Plane 1 in Fig. 1). As demonstrated in the depth profiles of these fault parameters (Figs 2f–h), the transitions between the different zones, in terms of these parameter values, are gradual. The effective normal stress below 5 km depth (10 km along dip distance) is a constant of 20 MPa (i.e. assuming over-pressurization) except within Z1 (50 MPa), and gradually decreases toward the free surface (Fig. 2g). Existence of fluid and fluid over pressurization, which give rise to low effective normal stress, are observed to be associated with slow earthquakes and slow slip events along subduction zones (Kimura *et al.* 2012; Kitajima & Saffer 2012; Bassett *et al.* 2014). Correspondingly, the initial shear fault stress is calculated as the product of normal stress and initial friction coefficient. We remark that these are initial fault stresses before simulations and they evolve spontaneously over multiple earthquake cycles.

Many variations of the base model can be designed to examine effects of the model parameters. In this study, we focus on the base model to quantitively test the conceptual model suggested from the observations of the historical tsunami earthquakes. We also construct additional models to demonstrate effects of various model parameters, and model parameters of these models are nearly the same as those in Model 1 except those explicitly given below. In Model 2, the main fault is longer along the strike (to 70 km) and the two asperities are further separated by the conditional stable zone. This model is to examine effects of the distance between the two asperities. In Model 3, we increase the a–b value from –0.002 to –0.001 in the conditional stable zone. This model is to examine effects of the property of the conditional stable zone (i.e. the degree of velocity-weakening). In Model 4 and 5, the main fault lengths are further extended to 120 km, with a larger conditional stable zone surrounding the two asperities of the same sizes as in Model 1. These two models are designed to explore rupture durations. We also simulate a fault model (i.e. Standard) in which the same value of a–b (–0.004) is distributed on the whole main fault, which

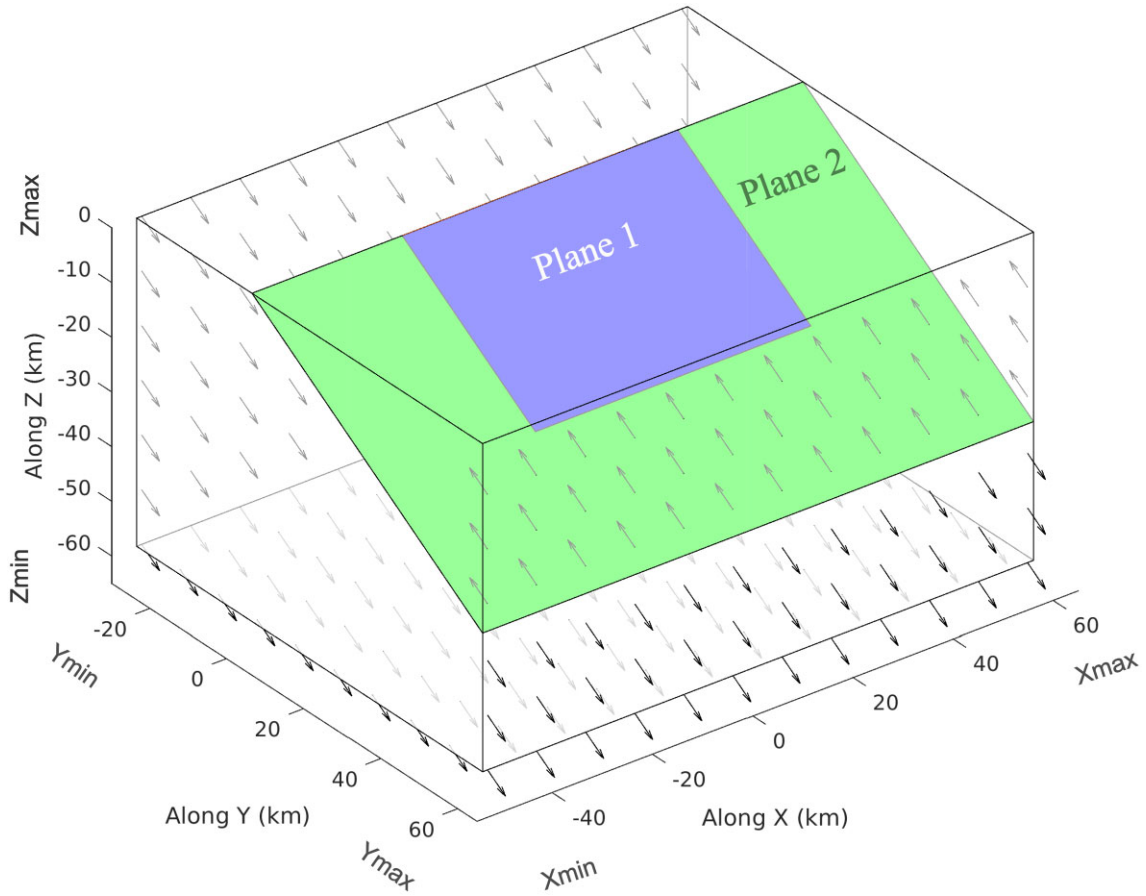

Figure 1. A schematic diagram that shows the 3-D thrust fault model, with dip angle of $\phi = 30^\circ$, and boundary conditions for the model. Plane 1 (blue) is the main fault with velocity-weakening frictional property that can host earthquake ruptures, which is surrounded by a velocity-strengthening area (Plane 2, green) that creeps. Top boundary is free surface. Left (Xmin) and right (Xmax) boundaries are fixed in x-direction, and are free in other directions. Half of the plate convergence rate is applied to the other boundaries as indicated by arrows, including front (Ymax), back (Ymin), and bottom (Zmin) boundaries, according to thrust faulting, to load the model.

Table 1. Basic model parameters in this study.

Parameters	Value
P wave speed, V_p	6000 m s^{-1}
S wave speed, V_s	3464 m s^{-1}
Shear modulus, μ	32 GPa
Poisson's ratio, ν	0.25
Density, ρ	2670 kg m^{-3}
Reference slip velocity, V_0	10^{-6} m s^{-1}
Steady state friction coefficient, f_0	0.6
Loading rate, V_{pl}	10^{-9} m s^{-1}
Element edge length in x direction, Δx	200 m
Time step (dynamic simulation)	0.005 s

results in ordinary earthquakes for a comparison with the tsunami earthquakes simulated in this study. In Model 6, there are two LNS asperities located downdip of one HNS asperity in order to explore interactions among several asperities.

There are several considerations in setting up the parameters on the fault. First, a velocity-weakening zone must be larger than the critical nucleation patch size h^* for earthquakes to occur within the zone. An estimate of the nucleation size h^* for 3-D mode II earthquakes (Rubin & Ampuero 2005; Chen & Lapusta 2009) is:

$$h^* = \frac{\pi}{2} \frac{\mu b L}{(1-\nu)(a-b)^2 \sigma} \tag{3}$$

where L, a, b and σ are the parameters as in eq. (1), μ and ν are shear modulus and Poisson's ratio, shown in Table 1. Given the parameter values discussed above, h^* is about 13 km for both the HNS and LNS asperities, and the size of them (14 km) is a little larger than h^* so that earthquakes can nucleate on them. The reason for us to choose a larger L (10 mm) for HNS compared with L (4 mm) for LNS is to make h^* the same because of higher effective normal stress 50 MPa on HNS compared with 20 MPa for LNS.

Second, one needs to resolve the cohesive zone near the rupture tip during the dynamic rupture process (e.g. Day *et al.* 2005). Within this zone, shear stress and slip rate vary dramatically and resolving this zone is critical for simulating dynamic rupture propagation. For numerical methods such as FEMs, this requires several elements within the cohesive zone, and thus imposes a constraint on the element size of a model (Day *et al.* 2005; Duan & Day 2008). On the other hand, reducing element size can significantly increase computational cost in 3-D modelling, and therefore we need to strike a balance between the model size and the element size. This consideration also plays an important role in our choice of parameter values above. The size of the cohesive zone Λ_0 for mode II earthquakes under the RSF law can be estimated as (Lapusta & Liu 2009):

$$\Lambda_0 = C_1 \frac{\mu L}{(1-\nu) b \sigma} \tag{4}$$

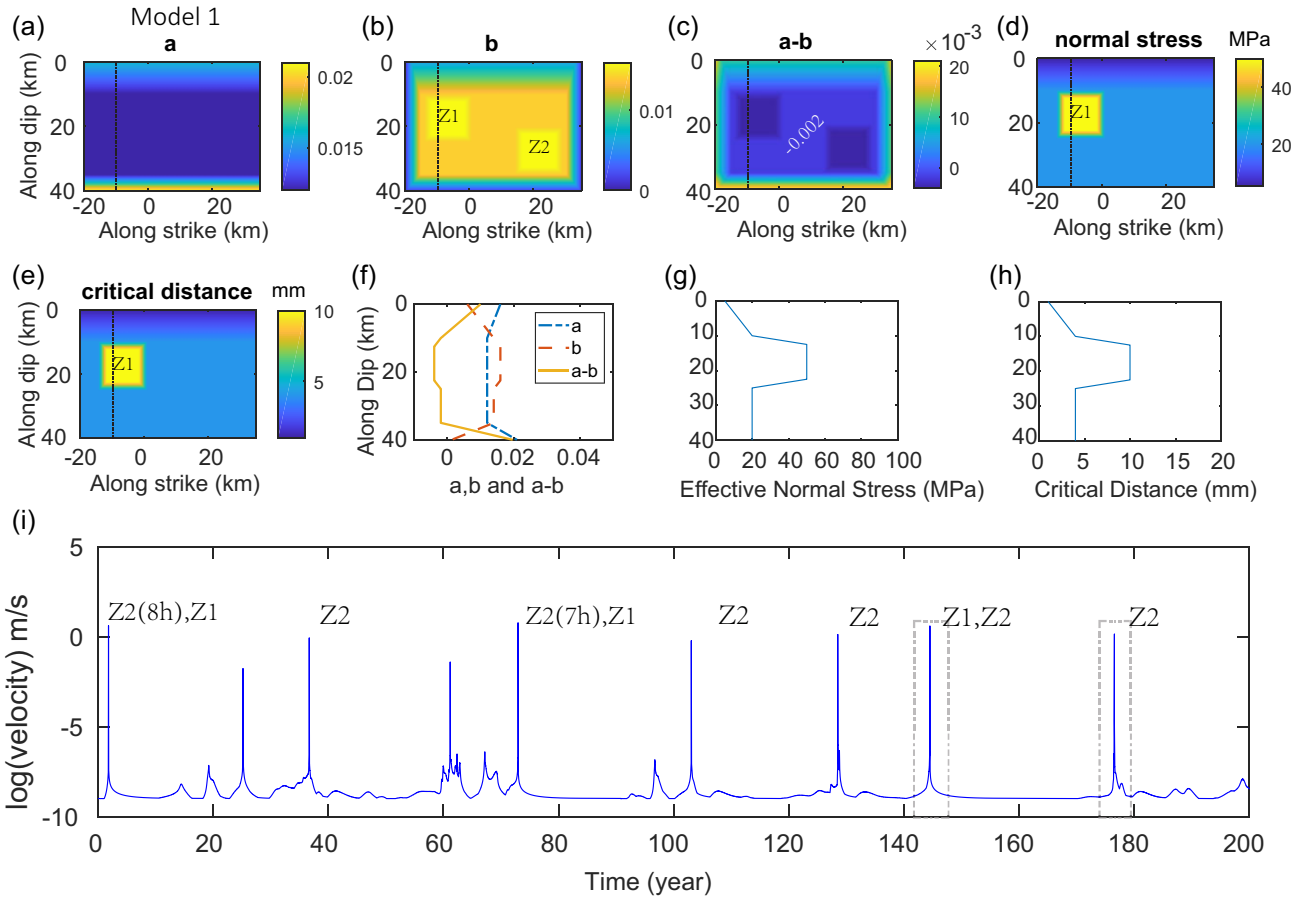

Figure 2. Distributions of model parameters on the main fault (Plane 1 in Fig. 1) for Model 1. (a), (b), (c) are a, b and a–b in the rate-and-state friction law, respectively. (d) effective normal stress. (e) characteristic slip distance L. (f), (g) and (h) show these parameters along a depth profile indicated by a black dashed line in (a)–(e). In this model, two unstable patches Z1 and Z2 with a–b of –0.004 are embedded in a conditionally stable zone with a–b of –0.002. Z1 (HNS) has a high effective normal stress of 50 MPa, while other parts of the fault plane have a low effective normal stress of 20 MPa, including Z2 (LNS). (i) Simulated maximum slip rate on the fault over multiple earthquake cycles in the model over 200 yr, showing various slip behaviours, including different rupture patterns in the earthquakes. High slip rate peaks ($\sim$1 m s^{-1}) represent the earthquakes and they are labeled by the asperities on which a dynamic rupture nucleates and/or propagates, with the delayed hours between two ruptures labeled in parentheses for example 7 hr (7 h) or 8 hr (8 h). Usually, the maximum slip rate mainly occurs over two asperities instead of the conditionally stable zone on the fault plane. Circled by two dashed boxes are two earthquakes that initiate from Z1 and Z2, respectively, with further analyses shown in Figs 3 and 4.

where C_1 is a constant, equal to $9\,\pi/32$ if the stress traction distribution is linear within the cohesive zone. For the given parameter values above, the element size of $\Delta x = 200$ m used in this study will give a ratio of $\frac{\Lambda_0}{\Delta x}$ $\sim$2.4 for dynamic ruptures on the HNS and LNS asperities, which resolves the cohesive zone (Day *et al.* 2005; Duan & Day 2008).

Finally, we also need to consider time steps in earthquake cycle simulation that also exert an important control on computational cost. For the dynamic phase, it requires that the length of the time step Δt should be restricted by the Courant–Friedrich–Lewy (CFL) condition (Courant *et al.* 1967), in order to keep the numerical simulation stable. For the quasi-static phases of an earthquake cycle, the length of the time step varies to ensure both computational efficiency and numerical stability, as the slip rates evolve on the fault (Luo *et al.* 2020).

4 RESULTS

We first present the results of earthquake cycle simulations from the base Model 1, focusing on earthquakes generated spontaneously over multiple earthquake cycles, in particular comparing features of these earthquakes with the observations from the historical tsunami earthquakes reviewed in the Introduction section. Then we discuss the results from Model 2 and Model 3, focusing on changes from Model 1 to demonstrate effects of the seperation distance between asperities and friction property of the conditional stable zone. In addition, we designed three other models (Model 4, Model 5 and the Standard model) to explore the normalized duration of simulated events. Finally we examine interactions of three asperities from Model 6.

4.1 The base Model 1: earthquakes nucleated from the HNS and LNS asperities

We examine the rupture pattern, recurrence interval, rupture speed, final slip, moment rate, stress drop, and induced coseismic seafloor displacement and velocity of earthquakes over multiple earthquake cycles from this model in this subsection.

4.1.1 Earthquake pattern and recurrence interval

Fig. 2(i) provides an overview of the earthquake sequence from the base Model 1 over ~200 yr. A maximum slip rate on the order of 0.1 m s^{-1} or larger in this plot indicates a seismic event, while maximum slip rates on the order of the loading rate 10^{-9} m s^{-1} suggest relatively steady-state interseismic phases. A maximum slip rate well above the loading rate, but below the seismic rate, suggests some slow-slip events from the model. We focus on the seismic events as labelled by the asperities on which a dynamic rupture nucleates and/or propagates. We can identify seven earthquake sequences (counting two continuously ruptured events delayed by hours as one earthquake sequence). We find that LNS Z2 ruptures more frequently than HNS Z1 and Z1 has a longer recurrence interval of ~75 yr than Z2 (~30 yr on average). These features appear to be related to the difference in effective normal stress between Z1 and Z2, suggesting that effective normal stress may modulate rupture nucleation and recurrence interval. Higher effective normal stress on Z1 makes it stronger and requires a longer time of loading for rupture nucleation, compared with Z2.

4.1.2 Rupture speed and slip

Fig. 3 shows characteristics of two representative events (indicated by dashed boxes in Fig. 2i) from the earthquake sequence. The bigger event that nucleates on Z1 also ruptures Z2, while the smaller one that nucleates on Z2 does not break Z1 in the event. For the given value of $a–b = –0.002$ in the conditionally stable zone, all ruptures nucleated on either Z1 or Z2 can continue propagating into the conditionally stable zone, though no earthquake can nucleate within the zone. In the two events, the average rupture speed is slow, ~1.9 km s^{-1} in the former (Fig. 3a) and ~1.3 km s^{-1} in the latter (Fig. 3b), comparable with observed rupture speeds in historical tsunami earthquakes. Relatively large slip occurs on the asperities, with a maximum final slip of about 2 m on Z1 in the bigger event (Fig. 3c) and a smaller maximum final slip of about 0.8 m on Z2 in the smaller event (Fig. 3d), while slip in the conditonally stable zone is small.

4.1.3 Moment release

The contrast in slip between the asperities and the conditionally stable zone is also reflected in seismic moment rate (Figs 3e and f). The bigger event has two discrete moment rate peaks, corresponding to rupture of the two asperities. The smaller event only has one moment-rate peak, corresponding to rupture of LNS asperity Z2. Moment release from the conditionally stable zone is low in both events. The total released moment in the bigger event is 4.59×10^{19} Nm, corresponding to M_w 7.05. It is 1.47×10^{19} Nm in the smaller event, corresponding to M_w 6.72. Multiple discrete moment rate peaks have been observed in the 2006 Java tsunami earthquake, and the inverted finite fault slip model for this M_w 7.8 earthquake shows that several asperities are separated tens of kilometres from one another near the trench and have been ruptured one by one from the east to the west (Ammon *et al.* 2006). The bigger event in our model shows that this feature in tsunami earthquakes can be generated from ruptures of discrete asperities within a conditionally stable zone under favourable conditions, including (1) the conditionally stable zone can sustain spontaneous rupture and (2) discrete asperities are ready to be ruptured (e.g. shear stress level is close to shear strength).

4.1.4 Stress drops

The average stress drop values from the two events are low (Figs 3g and h). It is 1.26 MPa in the bigger event and 0.90 MPa in the smaller event. Even though the stress drop value over the asperity Z1 is as high as 10 MPa, the stress drop on the conditionally stable zone is very low, resulting in the low average stress drop. Low stress drop has been observed in historical tsunami earthquakes. Kikuchi & Kanamori (1995) analyzed the broad-band body waves of the 1992 Nicaragua tsunami earthquake and found that the average stress drop was 1.1 MPa. Abercrombie *et al.* (2001) inverted the coseismic slip pattern of the 1994 Java earthquake and calculated that the average stress drop was as low as 0.3 MPa. In addition, we find that the stress drop distributions are very complex after two dynamic events, shown in Figs 3(g) and (h), that several oval shape stress drop circles exist on the fault plane. The stress distribution before a dynamic event is heterogeneous because of slip history including earthquakes, afterslip and slow slip events. The stress drop on Z1 asperity is much higher than that on Z2 asperity, which might be related with a higher effective normal stress on Z1. The stress drop difference can also help explain the longer earthquake recurrence interval on Z1 asperity than Z2, as the recurrence time interval is proportional to (stress drop)/(stress loading rate) and stress loading rate may be assumed a constant.

4.1.5 Seafloor displacement

Fig. 4 shows the maximum seafloor displacements and velocities at selected stations generated in the two representative events from the model. For the bigger earthquake nucleating on Z1, the maximum vertical displacement and velocity are 0.52 m and 0.18 m s^{-1} (Figs 4a and b), respectively, and strong vertical displacement is observed over a large area, which would contribute to tsunami generation. In addition, the earthquake ruptures through the shallow velocity strengthening zone all the way to the seafloor (Fig. 3a), resulting in horizontal seafloor displacment and veloicty perpendicular to the trench (along *Y*-axis) of as high as 0.40 m and 0.21 m s^{-1}, which could trigger landslide near the trench and contribute to tsunami generation. For the smaller earthquake nucleating on Z2, the maximum vertical displacement and velocity are 0.22 m and 0.04 m s^{-1} (Figs 4c and d), respectively, and relatively a smaller area on the seafloor has experienced strong veritcal displacement. It appears that rupture of the shallow HNS asperity contributes signiciantly to both vertical and horizontal seafloor displacements, and thus tsunami generation. In addition, a uniform velocity structure is used in this study to focus on heterogeneous friction and effective normal stress effects. If a shallow lower velocity layer is adopted in the model, seafloor displacement would be larger, increasing the potential of tsunami generation.

4.1.6 HNS as both barrier and asperity

From the earthquake cycle simulation, we found the HNS asperity acts as not only an asperity in some earthquakes (e.g. three out of the seven), but also a barrier in other earthquakes (e.g. four out of the seven). It is the same asperity in terms of its geometry (e.g. size) and frictional properties (e.g. a, b and L in RSF), but it can act as both an asperity and barrier to earthquake ruptures in its life span. This is likely due to different stress conditions spontaneously evolved over earthquake cycles. Whether or not a rupture can break a high-strength patch is sensitive to local conditions that vary with time due to past rupture and loading history. Theoretically, this imposes

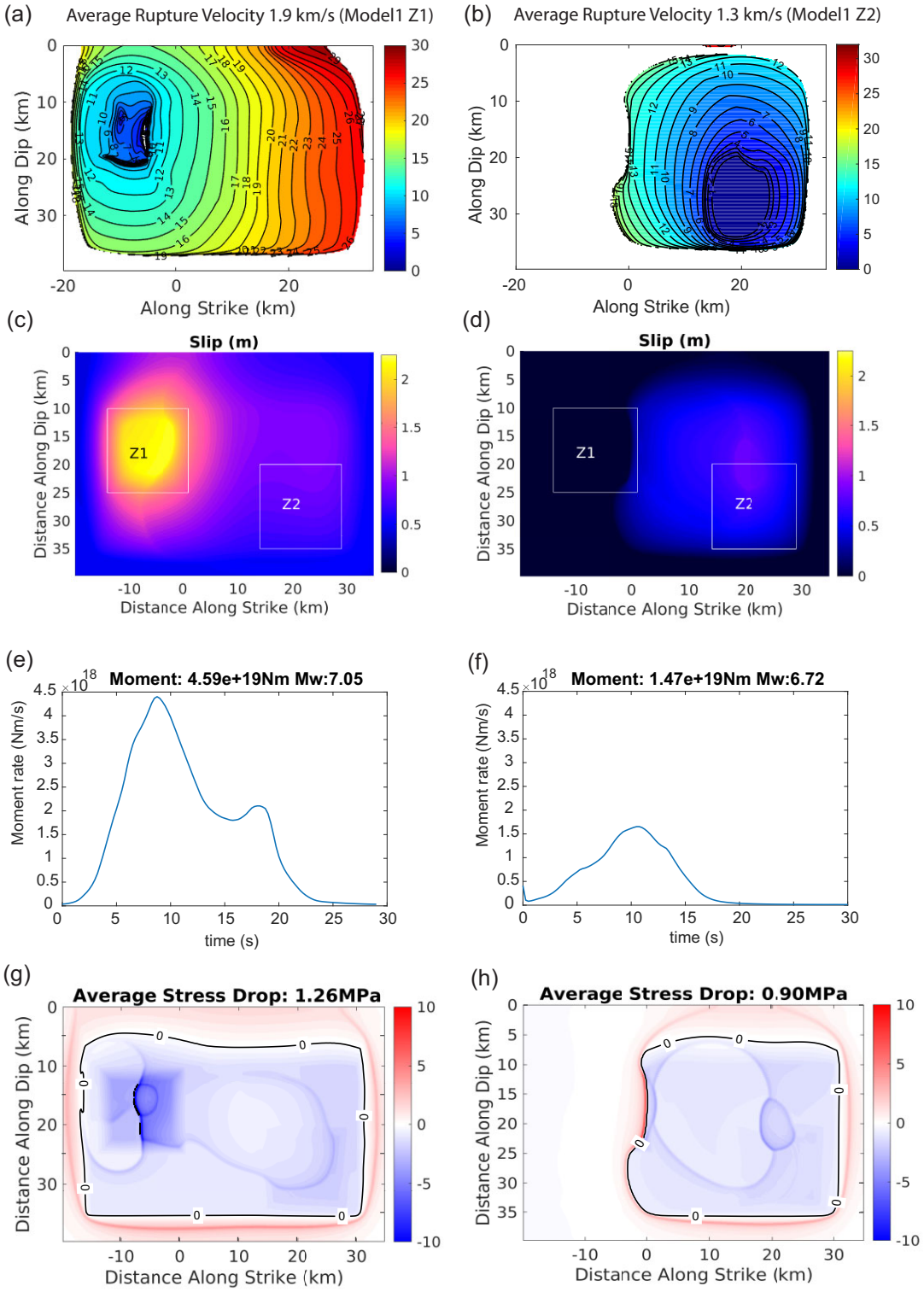

Figure 3. Rupture propagation, slip distribution, moment rates and stress change distribution of two earthquakes in Model 1 (illustrated by dashed boxes in Fig. 2i). Panels (a) and (b) coseismic rupture time contours in seconds, panels (c) and (d) coseismic final slips, with two white boxes representing the locations of Z1 and Z2 asperities, panels (e) and (f) released moment rates and panels (g) and (h) shear stress changes (negative as stress drops distributed within the zero stress change contours) for the earthquake nucleated on Z1 HNS asperity and ruptured Z2 cascadingly during the 144th year (left-hand panel) and for the earthquake nucleated on Z2 LNS asperity during the 176th year (right-hand panel) (Fig. 2i), respectively.

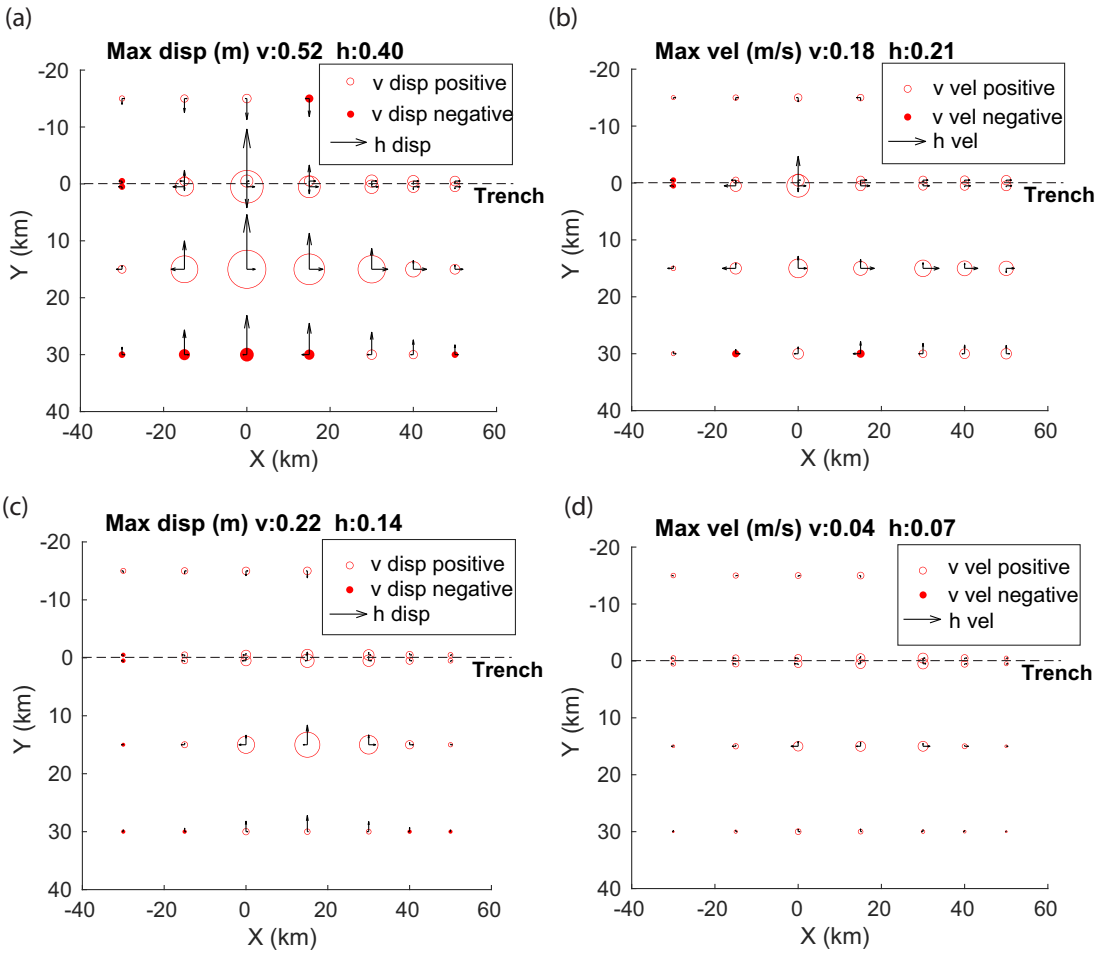

Figure 4. Seafloor deformation from two earthquakes in Model 1 (illustrated by dashed boxes in Fig. 2i). Panels (a) and (b) maximum seafloor displacement and velocity for the earthquake nucleated on Z1 HNS asperity in Model 1 and panels (d) and (e) show maximum ground surface displacement and velocity for the rupture nucleated on Z2 LNS asperity in Model 1. The horizontal dashed lines represent the trench separating the hanging wall and footwall. Letters h and v in the legends denote the ground surface parallel and ground surface vertical motions, respectively.

a significant limit to our ability to predict earthquakes (and also earthquake early warning) in terms of their final sizes. But what we may achieve is to understand possible rupture scenarios and patterns from physics-based modelling of earthquake cycles such as one in this study. By comparing modelled results against observations such as seismicity patterns, we may still be able to assess likelihood of a larger versus smaller earthquake on a fault system.

4.2 Effects of separation distance between asperities and friction properties of the conditionally stable zone

Figs 5 and 6 show parameters of Model 2 and Model 3, and the earthquake sequences from them, respectively. In Model 2, the fault is extended along the strike and the two asperities are 15 km further apart along the strike than in Model 1. In Model 3, the a–b value is increased to –0.001 for the conditionally stable zone (thus closer to zero) from –0.002 in Model 1. Figs 7 and 8 show rupture characteristics and seafloor displacements of one earthquake from Model 2 and Model 3 (labelled by dashed boxes in Figs 5 and 6), respectively.

4.2.1 Separation distance between asperities

Compared with Model 1, Model 2 shows that the larger horizontal distance between the two asperities has minor effects on recurrent interval (Fig. 5e), average rupture velocity (Fig. 7a), and maximum slip (Fig. 7b) on the fault. The two peaks of moment rate are separated further in time (Fig. 7c) and strong seafloor displacement is distributed over a larger area (Fig. 7d) in Model 2 because of the longer fault dimension. The total moment release in Model 2 is not significantly larger than that in Model 1 (Fig. 7c), which is consistent with a weak contribution to moment release from the conditionally stable zone. The moment magnitude of this event in Model 2 is M_w 7.11.

4.2.2 Friction properties on the conditionally stable zone

Model 3 shows that the degree of velocity-weakening in the conditionally stable zone has obvious effects on rupture characteristics and seafloor displacement. The recurrence intervals of earthquakes on Z1 and Z2 are about 58 and 22 yr, respectively, in Model 3 (Fig. 6e), which are shorter than those in Model 1 (about 75 and 30 yr, respectively, Fig. 2i). This is understandable in the sense that a weaker velocity-weakening conditionally stable zone may creep at a larger rate and thus loads the two asperities more rapidly. For

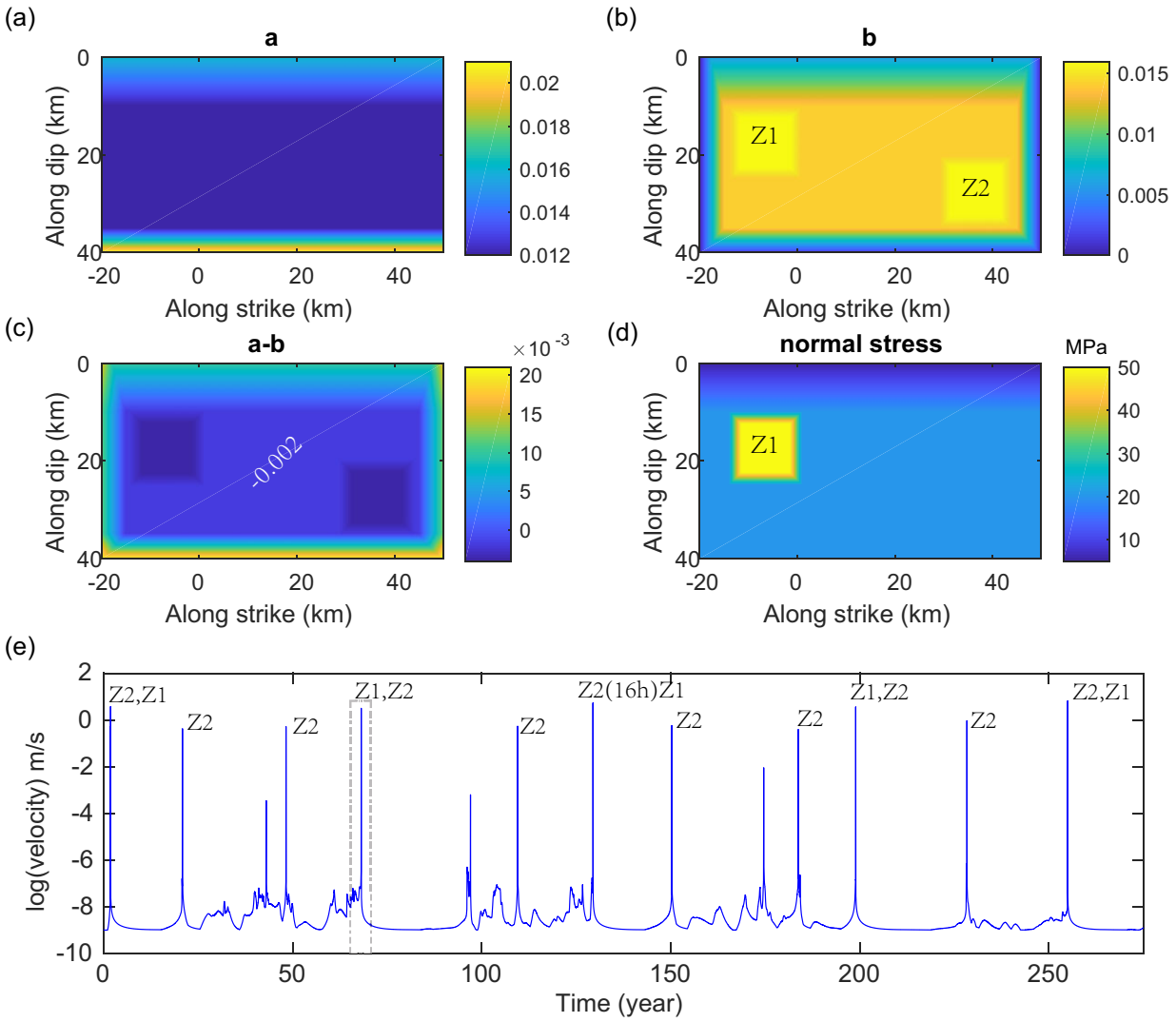

Figure 5. Model parameters on the fault and simulated earthquake sequences in Model 2. (a) *a* value, (b) *b* value, (c) *a*–*b* value and (d) effective normal stress. (e) Simulated maximum slip rate on the fault over earthquake cycles. The dashed line box is an earthquake that initiates from Z1 at the 68th year, with more details shown in Fig. 7. The two patches Z1 and Z2 are separated further apart in Model 2 than in Model 1.

the weaker velocity-weakening conditionally stable zone, even the rupture nucleated from the HNS asperity propagates very slowly at an average speed of about 1.2 km s^{-1} (Fig. 8a) and the rupture propagation spontaneously ceases within the conditionally stable zone. This makes the cascade failure of several asperities difficult to happen within one event. The maximum final slip of this earthquake is about 1.8 m (Fig. 8b), smaller than the final slip of 2.2 m of the relatively large earthquake in Model 1. In addition, the earthquake magnitude (M_w 6.8) and total moment (Fig. 8c) are lower than those of the earthquake in Model 1 (Fig. 3e), because the rupture size is limited due to a weaker velocity weakening conditionally stable zone. Correspondingly, the seafloor displacement is relatively smaller within a smaller area (Fig. 8d).

4.3 Normalized source duration and spectrum of tsunami earthquakes

4.3.1 Normalized durations of historical tsunami earthquakes

To compare source durations of different sizes of tsunami earthquakes, previous studies have proposed to use the normalized source duration, which is calculated by dividing the source duration of an earthquake with the cube root of its moment M_0, normalized to an $M_w = 6.0$ event (Kanamori & Anderson 1975; Houston *et al.* 1998; Campus & Das 2000; Bilek & Lay 2002). We calculate the normalized durations for well-studied historical tsunami earthquakes occurred along Japan, Alaska, Peru, Kuriles, Nicaragua, Java and Mentawai margins based on their estimated source durations and moments (Table 2) and plot them in Fig. 9(a). The observed range of the normalized duration for these tsunami earthquakes is from 9 to 23 s (Fig. 9a), much higher than the standard subduction zone thrust mechanism earthquakes of around 5 s (Bilek & Lay 2002; Bilek & Engdahl 2007). We remark that the source time functions of these well-known historical tsunami earthquakes are usually composed of several discrete moment rate release peaks, suggesting

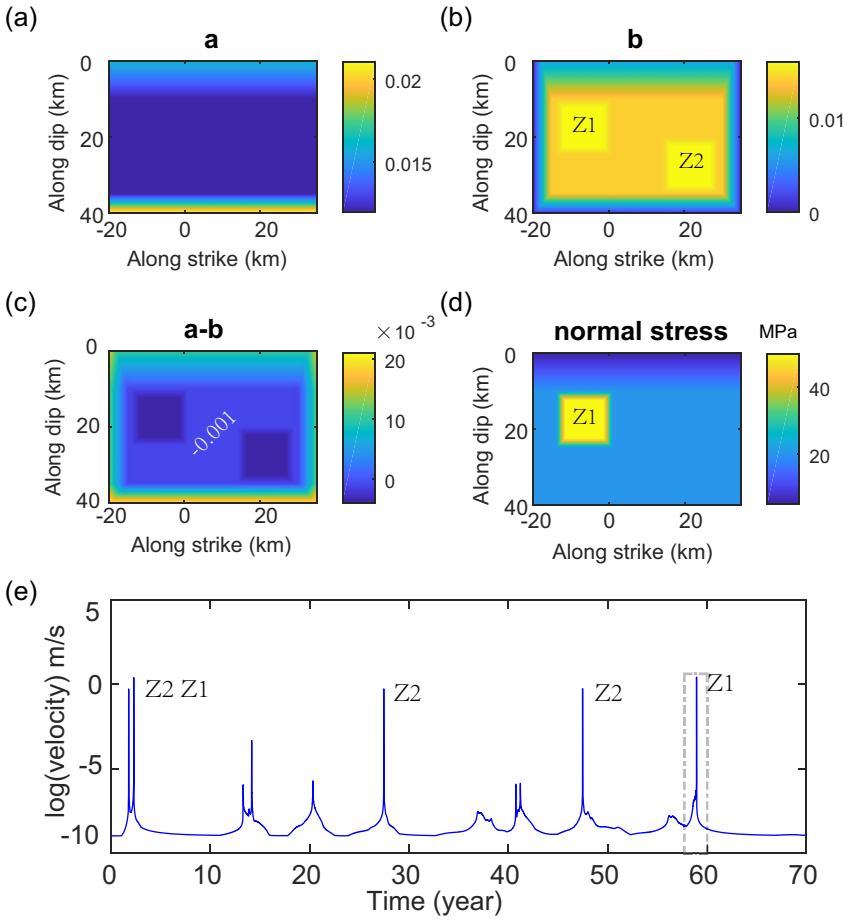

Figure 6. Model parameters on the fault and simulated earthquake sequences in Model 3. (a) *a* value, (b) *b* value, (c) *a*–*b* value and (d) effective normal stress. (e) Simulated maximum slip rate on the fault over earthquake cycles. The dashed line box is an earthquake that initiates from Z1 at the 59th year with more details shown in Fig. 8. In Model 3, the *a*–*b* value in the conditionally stable zone increases to –0.001 from –0.002 in Model 1.

ruptures on a series of asperities within the conditionally stable zone (Abercrombie *et al.* 2001; Ammon *et al.* 2006; Lay *et al.* 2011).

4.3.2 Normalized durations in our models

We run more models with various fault dimensions and *a*–*b* values in the conditionally stable zone to explore the normalized source duration of earthquakes in our models. Fig. 10 shows three of them. Model 4 and Model 5 have a larger dimension of the main fault than Models 1–3, with different configurations of the two patches Z1 and Z2 between the two models. The *a*–*b* value within the conditionally stable zone in Models 4 and 5 is the same as that in Models 1 and 2 (i.e. –0.002). Model 'Standard' is a reference model for an ordinary earthquake with an *a*-*b* value of –0.004 on the entire main fault. In conducting our numerical experiments, we find that the normalized source duration of the simulated earthquakes in our models is very sensitive to the *a*–*b* value within the conditionally stable zone. We test the *a*–*b* values of –0.004, –0.003, –0.0017, –0.0015 (models not shown), in addition to –0.002 and –0.001 in the above models. The normalized source durations from these models are summarized in Fig. 9(b), which clearly shows that for the models we run in this study, using *a*–*b* value of –0.002 to –0.003 can reproduce long normalized source durations observed in historical tsunami earthquakes with a range from 9 to 23 s. All other values of *a*–*b* produce the normalized source duration at or below the minimum value observed in historical tsunami earthquakes. We can understand these results by some qualitative analyses. When *a*–*b* is low (–0.004) on the conditionally stable zone, the fault zone is more velocity weakening, which results in a fast rupture propagation, similar to an ordinary earthquake with a low normalized source duration. When *a*–*b* is high (e.g. –0.0017, –0.0015 and –0.001) on the conditionally stable zone, the fault zone is more velocity strengthening, which strongly inhibits the rupture propagation and also results in a low normalized duration. We remark that the narrow range of *a*–*b* here corresponds to the model parameter values in this set of models, including normal stress and *L* values, etc. If we use different values of other parameters, the range of (*a*–*b*) may be different. In addition, the narrow range may allow us to place a good constraint on this parameter from observations if other parameters can be constrained by other means.

4.3.3 Difference in source durations

Here we provide more detailed analyses on rupture propagation and source duration of earthquakes from the three models shown in Fig. 10. Model 4 is based on Model 2 and the main fault is further extended to 120 km with a larger conditionally stable zone to the right of the LNS asperity (Fig. 10a). We intend to set up an environment that earthquakes could unilaterally rupture from the

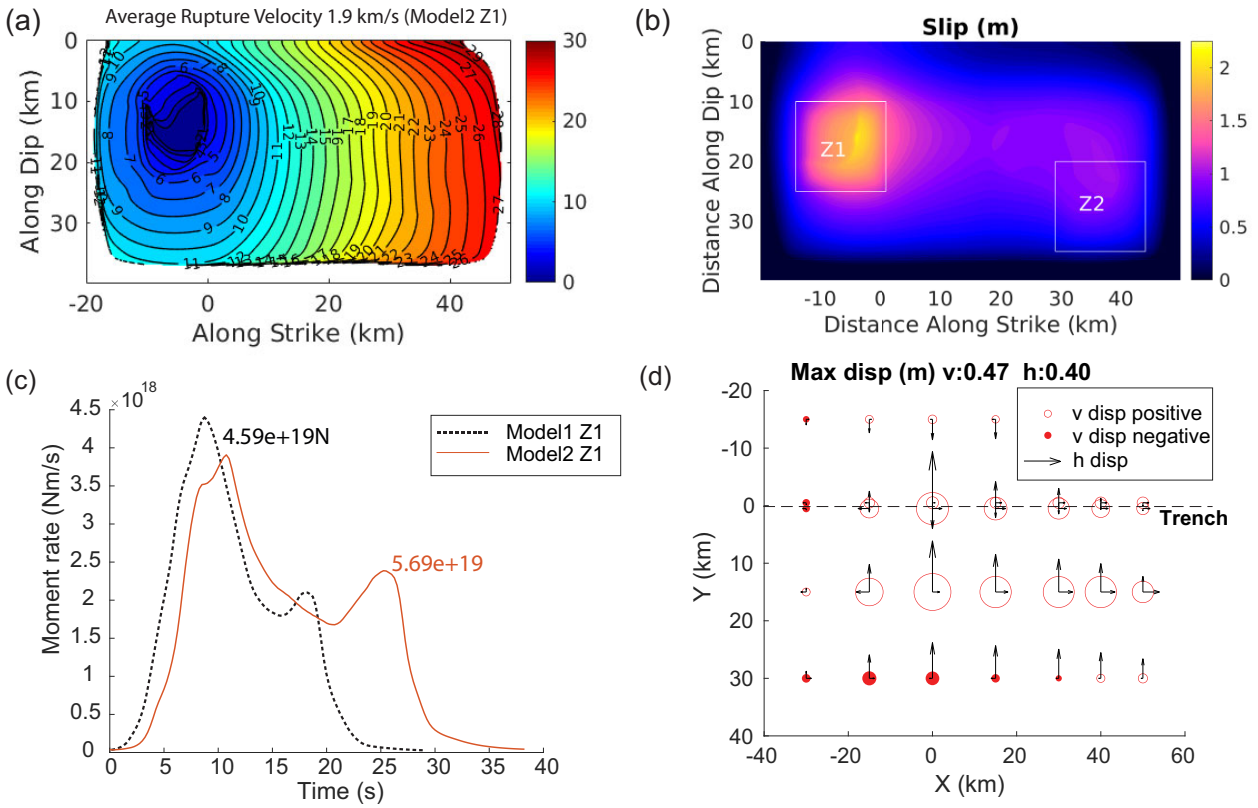

Figure 7. Rupture characteristics and seafloor displacement of an earthquake (indicated by a dashed box in Fig. 5e) from Model 2. (a) Rupture time contour in seconds, (b) coseismic slip in meters, with two white boxes representing the locations of Z1 and Z2 asperities, (c) released moment rate and (d) maximum seafloor displacement. Black dashed curve in (c) is moment rate of the earthquake nucleated on Z1 in Model 1 (i.e. shown in Fig. 3e) for comparison with the earthquake in this model (red curve).

HNS asperity Z1 to the LNS asperity Z2 and further to the right into the conditionally stable zone for a long source duration. However, earthquakes that ruptured Z1 and Z2 asperities are not able to propagate much into the conditionally stable zone, resulting in a low normalized source duration of about 10 s, near the low end of the observed range, as shown by the red solid circle in Fig. 9(b). There are two close peaks of the moment release: the large one relating to the Z1 rupture and the small tail relating to the Z2 rupture (Fig. 11a), generating a compact source time function. In Model 5, the fault length is the same as in Model 4, but the Z1 and Z2 asperities are located at the same depth (along dip direction) and distributed symmetrically along the strike direction (Fig. 10b). For a representative event in Fig. 11(c), the rupture propagation results in a long-normalized source duration around 23 s near the high end of the observed range, shown by the red solid diamond in Fig. 9(b). This event has a long source time function (∼100 s) composing of two well-separated moment rate peaks released from ruptures on Z2 and Z1 (Fig. 11c), separated by 55 s in between. Due to the high fault strength on HNS asperity, the triggering process of the Z1 asperity is slow, which contributes to the long time interval (55 s) between the two subevents. In the 'Standard' model (Fig. 10c), the source time function is very compact and simple (composing of only one moment rate peak, Fig. 11e), resulting in a normalized source duration of only 5 s (Fig. 9b). The contrast in the source duration between Model 4 (Fig. 11a) and Model 5 (Fig. 11c) suggests that the configuration (distribution) of locally locked velocity-weakening patches is very important for tsunami earthquake generation, in particular for very long source duration events. A favourable distribution of these patches will allow a rupture to propagate continuously and slowly, resulting in a long source duration.

4.3.4 Spectra analysis

We also calculate the spectra for three simulated events discussed above, based on their source time functions, along with the reference spectra using ω-squared spectra under the same seismic moments and stress parameters of 3 MPa (Figs 11b, d and f). The simulated events in Model 4 and Model 5 are both depleted in short period moment relative to the reference spectra (Figs 11b and d), which is consistent with the observed tsunami earthquakes (Abercrombie *et al.* 2001; Ammon *et al.* 2006; Lay *et al.* 2011). Especially, for the simulated event in Model 5, the spectrum is even depleted at the frequency band lower than 0.01 Hz (Fig. 11d), resulting in a compound and unsmooth spectrum near low frequency. This characteristic is observed in the Java 2006 event (Ammon *et al.* 2006), and appears to be related to the discrete moment release peaks in the source time functions. On the other hand, the spectrum for the ordinary earthquake is much closer to the reference spectrum especially at frequency band lower than the corner frequency (Fig. 11f).

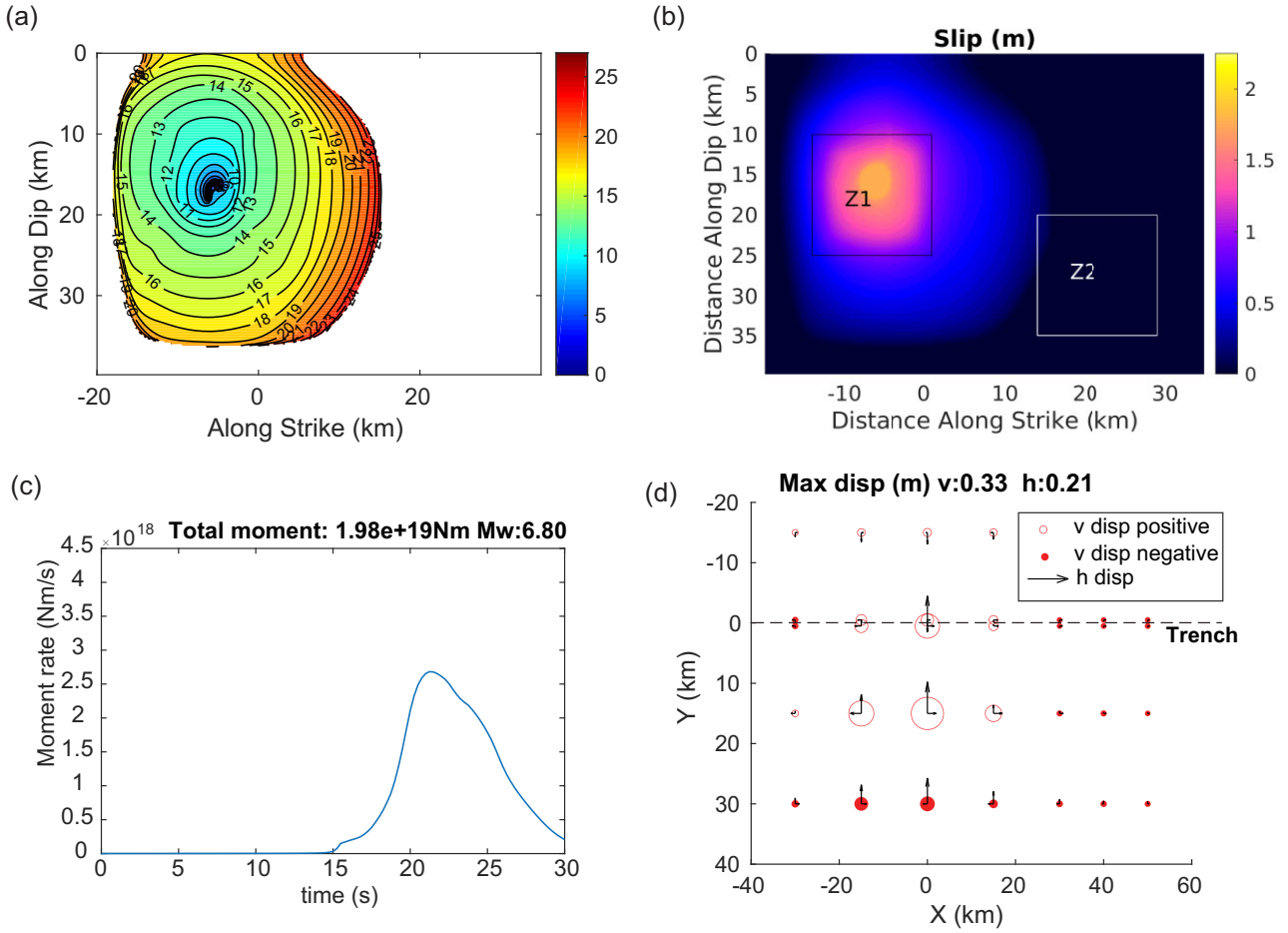

Figure 8. Rupture characteristics and seafloor displacement of an earthquake (indicated by a dashed box in Fig. 6e) from Model 3. (a) Rupture time contour in seconds, indicating an average rupture speed of around 1.2 km s^{-1} (b) coseismic slip in metres, with two boxes representing the locations of Z1 and Z2 asperities, (c) released moment rate and (d) maximum seafloor displacement.

Table 2. Source parameters for historical tsunami earthquakes.

No.	Region	Date	M_w	M_0 (Nm)	Duration (s)	Normalized duration (s)
1	Japan	1896/06/15	8.0	1.2e21	100	10.1
2	Alaska	1946/04/01	8.2	2.3e21	100–150	10.2
3	Peru	1960/11/20	7.6	3.4e20	125	19.3
4	Peru	1996/02/21	7.5	1.9e20	50	9.4
5	Kuriles	1963/1020	7.8	6.0e20	85	10.8
6	Kuriles	1975/06/10	7.5	2.0e20	80–100	16.6
7	Nicaragua	1992/09/02	7.7	4.2e20	125	18.0
8	Java	1994/06/02	7.6	3.5e20	85	10.2
9	Java	2006/07/17	7.8	6.7e20	185	23.3
10	Mentawai	2010/10/25	7.8	6.7e20	90	11.4

References: 1. Kanamori (1972); 2. Tanioka & Satake (1996); 3. Johnson & Satake (1997); 4. Pelayo & Wiens (1990); 5. Ihmlé *et al.* (1998); 6. Pelayo & Wiens (1992); 7. Ihmlé (1996); 8. Abercrombie *et al.* (2001); 9. Ammon *et al.* (2006) and 10. Lay *et al.* (2011)

4.4 Interaction between HNS and downdip LNS asperities

The 2010 M_w 7.8 Mentawai tsunami earthquake occurred up-dip of the 2007 M_w 7.9 earthquake (Lay *et al.* 2011), and the 2006 Java tsunami earthquake involved 5–6 pulses of moment release superimposed on a smooth rupture, suggesting multiple separated asperities were ruptured in the event (Ammon *et al.* 2006). These events demonstrate interactions among asperities distributed on subduction surfaces. Two asperities, which are separated mainly along the horizontal direction, may rupture in one event in the above models, in which earthquakes could initiate on either of the asperities. In Model 6, we add one more LNS asperity and arrange the two LNS asperities Z2 and Z3 to be downdip (on the two sides) of the HNS Z1 (Fig. 12) to examine interactions of multiple asperities, whereas

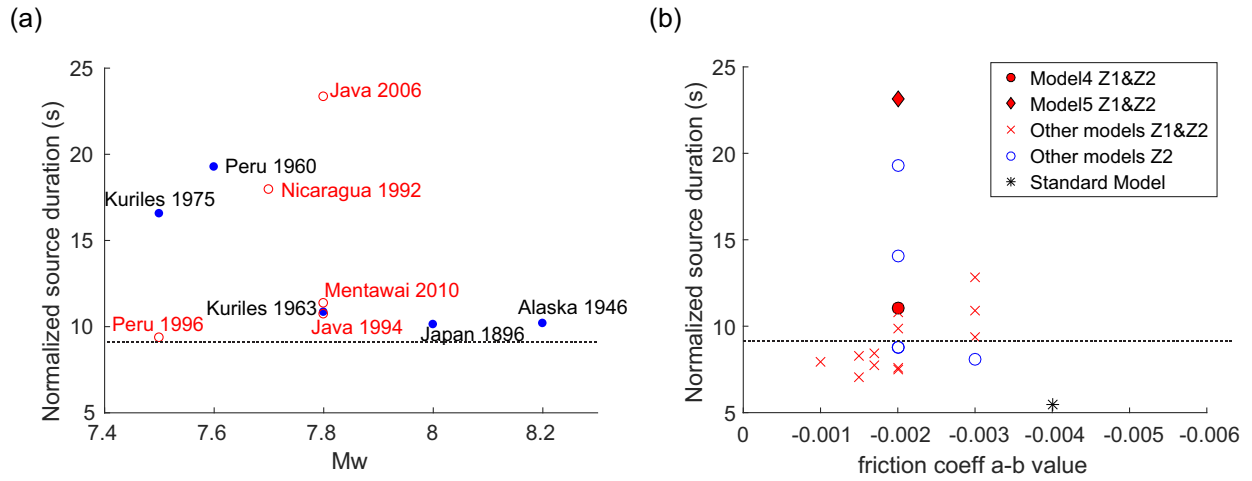

Figure 9. (a) Normalized source duration for historical tsunami earthquakes calculated based on their moment rates and durations listed in Table 2. Events labelled in red hollow circles are tsunami earthquakes occurred after 1990 that are better studied by the worldwide seismic network. (b) Normalized source duration for simulated tsunami earthquakes of various models in this study. The horizontal axis represents the *a*–*b* values used in the conditionally stable zone for the models. Blue hollow circles represent the simulated earthquakes that only rupture over asperity Z2 and get stopped by asperity Z1. All other symbols represent the simulated earthquakes that rupture both the Z1 and Z2 asperities in the models. Two cases (the red solid diamond and red solid circle) are shown in detail in this study. Black star represents an ordinary earthquake. Horizontal black dashed line in both (a) and (b) represents the minimum threshold of the normalized durations from historical tsunami earthquakes.

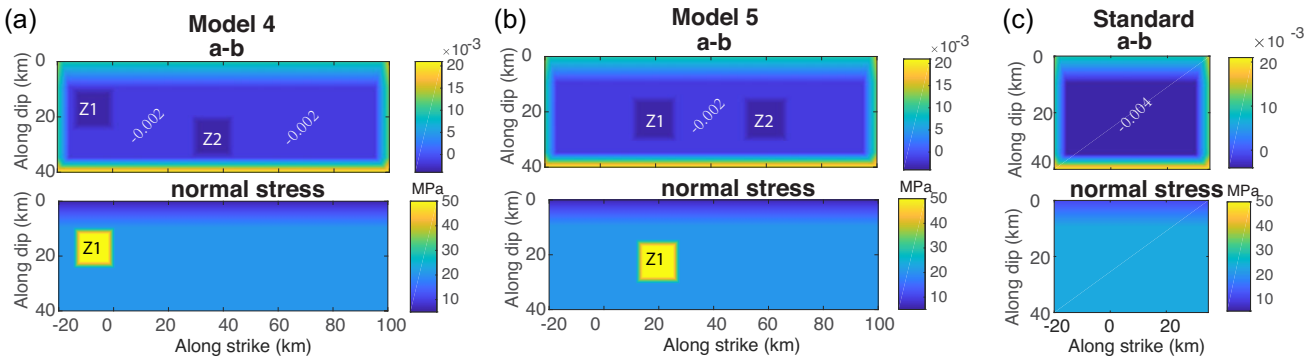

Figure 10. Parameters on fault in Model 4 (a), Model 5 (b) and Standard model (c), with *a*–*b* (top panel) and normal stress (bottom panel) for each model.

other aspects of Model 6 are the same as Model 1.

Fig. 12(e) shows earthquake sequences from this model over ~170 yr. It appears that two down-dip LNS asperities Z2 and Z3 can rupture more frequently. The recurrence interval on each of the two is about 20 yr, while the HNS Z1 is locked. About every 70 yr, the shallow HNS asperity Z1 can be triggered by ruptures on Z2 and/or Z3, with a time delay from several hours to several days, as shown at 2nd yr, 69th yr, and 149th yr (Fig. 12e). For example, in the 69th yr, a rupture first occurs on Z3. After ~4 d, Z2 ruptures, followed by a failure on Z1 then to the whole fault zone (including rerupture of Z3 and Z2). Fig. 13 shows some snapshots for this earthquake sequence. It appears the triggering of Z2 is caused by afterslip of the event on Z3. Although the event on Z3 4 d earlier could not trigger slip on the HNS Z1 immediately, its afterslip weakens Z1 (Fig. 13b). The rupture that starts on Z2 4 d later finally breaks the HNS Z1 (Fig. 13c), then propagates onto the entire fault, including the Z2 and Z3 asperities that just ruptured earlier (Fig. 13d).

5 DISCUSSION

Our models in which two or three asperities with unstable velocity-weakening properties are surrounded by a conditionally stable zone can reproduce slow rupture propagation and long normalized duration events, characteristic features of tsunami earthquakes. These results demonstrate that rupture of locally locked, unstable patches (asperities) within a conditionally stable zone at shallow part of subduction interfaces is a viable conceptual model for tsunami earthquake generation, and high normal stress asperities due to subducted seamounts can act as either barriers (stopping ruptures) in some events or 'true' asperities (rupturing with large slip) in other events.

It appears that asperities (locally locked, unstable patches) are important in tsunami earthquake generation within a conditionally stable environment at shallow depth. Otherwise, earthquakes cannot nucleate (and thus no earthquakes) in this environment. Furthermore, our models show that the value of *a*–*b* in the conditionally stable zone is also critical in tsunami earthquake propagation. Overall, it should be negative (thus velocity-weakening) to sustain rupture propagation. Within this range (<0), a smaller value (i.e. $a-b = -0.004$, indicating stronger velocity weakening) will result in events close to ordinary rupture propagation (i.e. at rupture speeds of ordinary earthquakes) while a larger value (i.e. $a-b = -0.0017$, -0.0015 or –0.001, implying weaker velocity-weakening) will slow down the rupture speed after rupture fronts propagates into this zone, and it is

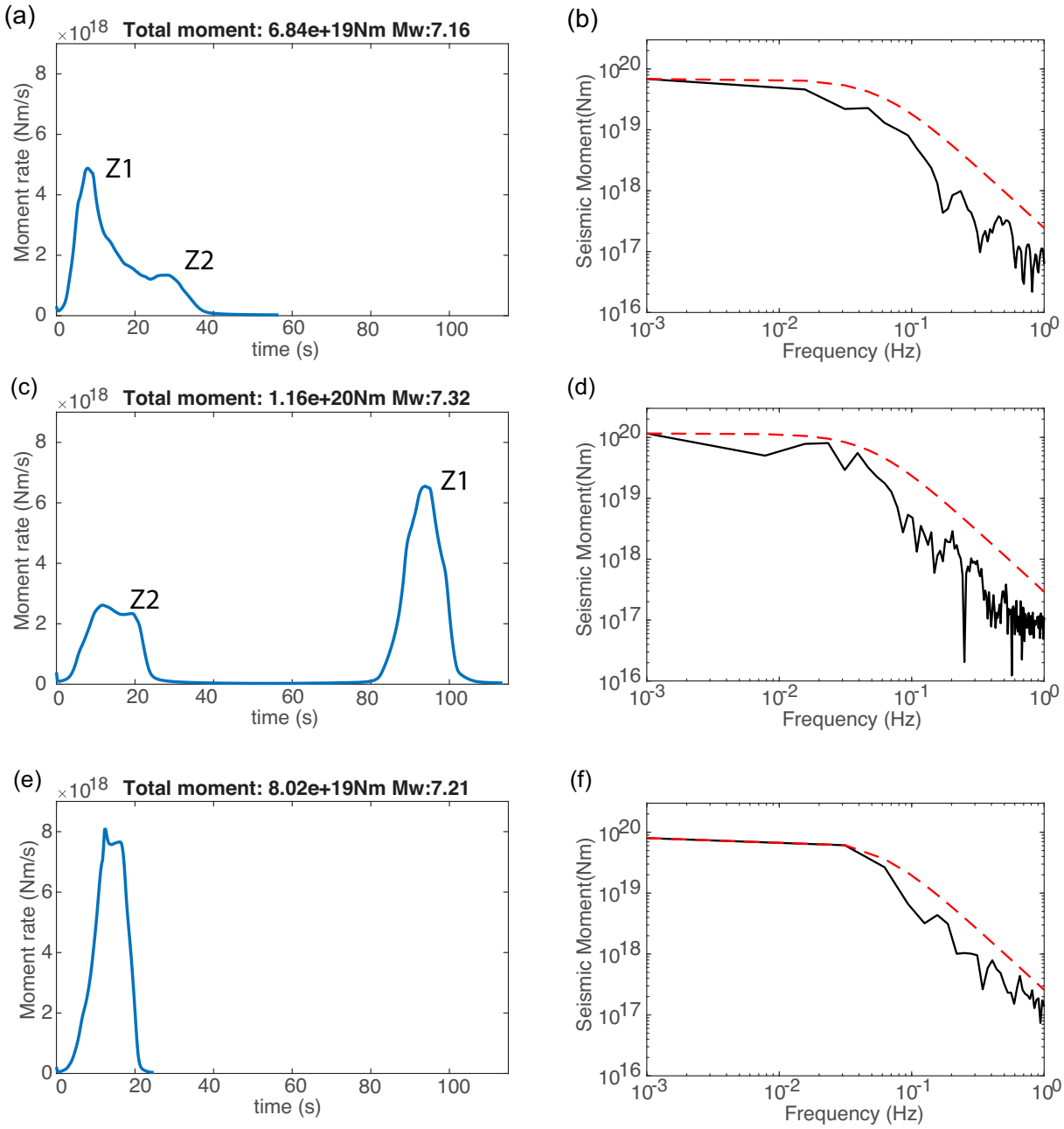

Figure 11. Moment rate and the corresponding spectra for earthquakes generated in Model 4, Model 5 and the Standard Model shown in Fig. 10. (a) The moment rate of an earthquake that initiates on Z1 and ruptures to Z2 in Model 4, with normalized duration of 11 s shown by the red solid circle in Fig. 9(b). (b) The black line represents moment spectrum calculated using the moment rate for the earthquake shown in (a). The red line is a reference spectrum for an ω-squared model with 3 MPa stress parameter for the seismic moment of 6.84e + 19 Mm shown in (a). (c) and (d) Moment rate and spectrum for an earthquake, in Model 5, that initiates on Z2 and triggers rupture on Z1 about 55 s later, with normalized duration of 23 s shown by the red solid diamond in Fig. 9(b). (e) and (f) Moment rate and spectrum for an earthquake, in the Standard model, that ruptures the whole fault zone with normalized duration of 5 s shown by the black star in Fig. 9(b).

more difficult to rupture several well-isolated asperities within one earthquake. These results also suggest that the dynamic earthquake simulator may be used to infer frictional properties on subduction interfaces by matching observations, such as slow rupture propagation and long source duration of tsunami earthquakes.

Model 6 demonstrates a complex rupture pattern among three asperities. If there are more asperities in a model than those in Model 6, we expect more complex interactions among asperities. In particular, under favourable conditions, a rupture may break a series of distributed asperities in a cascade fashion, resulting in a large event. The 2006 Java tsunami earthquake involves 5–6 pulses of moment release (Ammon *et al.* 2006), and these moment-release pulses may be an example of failure of a series of distributed asperities in a conditionally stable zone in one earthquake. From the results of Models 1–6 in this study, it's more likely for LNS asperities to fail in a cascade fashion, though the first asperity in the sequence may be a HNS asperity (Figs 2i and 12e) and occasionally a HNS asperity may fail later in the sequence (Figs 2i and 5e). Therefore, it's likely

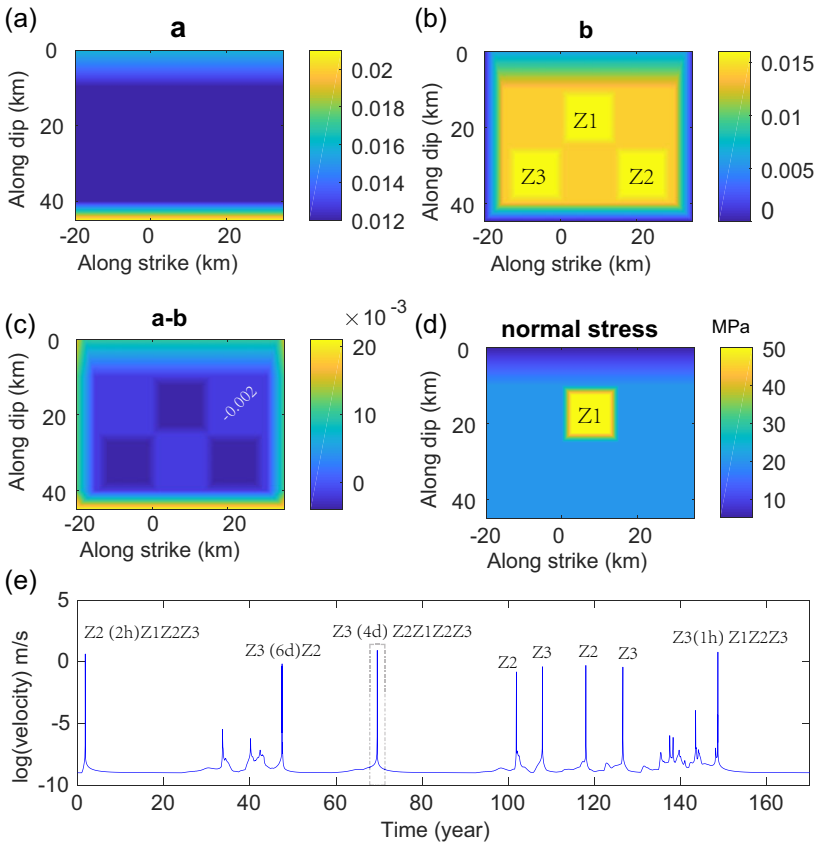

Figure 12. Model parameters on fault in Model 6 and simulated earthquake sequences from the model. (a) *a* value, (b) *b* value, (c) *a*–*b* value and (d) effective normal stress. (e) Maximum slip rate on the fault over earthquake cycles. The dashed box is a dynamic rupture (at the 69th year) that initiates from LNS asperity Z3 and then sequentially ruptured LNS asperity Z2 and HNS asperity Z1 4 days later. The snapshots of this rupture process are shown in Fig. 13.

the 5–6 asperities involved in the 2006 Java tsunami earthquake are mostly LNS asperities. However, these LNS asperities are not necessarily caused by lithified permeable sediments as conceptualized in our models. Because the rupture area is a region of complex bathymetry on the subducting plate (Ammon *et al.* 2006), they are likely low-relief topographic highs on the subducting interface, and thus more like the LNS asperities (because of low-relief) rather than the HNS in our models.

Our models show that an HNS asperity may act as an asperity in one earthquake but a barrier in another earthquake. For example, the HNS Z1 acts as a barrier in most of earthquakes, illustrated by events labeled by Z2 only (Fig. 2i). Even Z1 ruptures some hours after Z2 fails, Z1 still acts as a barrier so that an event on Z2 does not evolve into a larger one that ruptures both Z2 and Z1. This barrier effect of an HNS asperity may be its 'normal' role in earthquake generation on subduction interfaces. For example, the 2006 Java tsunami earthquake terminates just west of a large segment of uplifted topography (Bilek & Engdahl 2007), which may be an HNS formed by a subducted seamount. However, the HNS Z1 also acts as an asperity in some other events, illustrated by events labelled by Z1 (and Z2, Figs 2i and 11). Therefore, the same HNS may act as a barrier in some earthquakes but as an asperity in other events. Its 'normal' barrier role may lead to a misperception that it is aseismic, and thus an underestimation of the potential risk of earthquakes and tsunami hazards around such areas. Because of its barrier effect in many events, the recurrence interval of earthquakes on an HNS asperity is longer than that on other LNS asperities. The asperity role (i.e. its failure in earthquakes) of a HNS is clearly demonstrated in the 1994 Java earthquake (Abercrombie *et al.* 2001; Bilek & Engdahl 2007) and the 1947 Offshore Poverty Bay and Tolaga Bay earthquakes (Bell *et al.* 2014), and subducted seamounts may act as the HNS asperities in these events.

It is worth to further discuss the choices of the model parameter values in this study. As we point out earlier, the narrow range of *a*–*b* (i.e. –0.002 to –0.003) that quantitatively reproduces the observed normalized source durations of tsunami earthquakes corresponds to the chosen values of the other model parameters in this set of models, including normal stress and *L* values etc. For example, if we choose different values of the effective normal stress (e.g. higher than 20 MPa for most part of the subduction plane), the range of *a*–*b* on the conditional stable region to reproduce the observed source durations of tsunami earthquakes could be slightly different. However, the conclusion about a narrow range of *a*–*b* for the observed source durations will hold.

We use a uniform velocity structure in the elastic models of this study to focus on effects of heterogeneous stress and frictional properties. If typical subduction zone structure is included, such as low-velocity shallow layers (in particular accretionary prisms at accretionary margins), we expect larger seafloor displacement, and thus greater tsunami generation potential than our models show. Several former studies have shown that the low elastic moduli and wave speeds of hanging wall materials could also cause a long duration of tsunami earthquakes (Ma & Beroza 2008; Lotto *et al.* 2017; Lotto *et al.* 2018; Sallares & Ranero 2019; Sallares *et al.* 2021). In addition, potential plastic yielding in low-velocity accretionary prisms

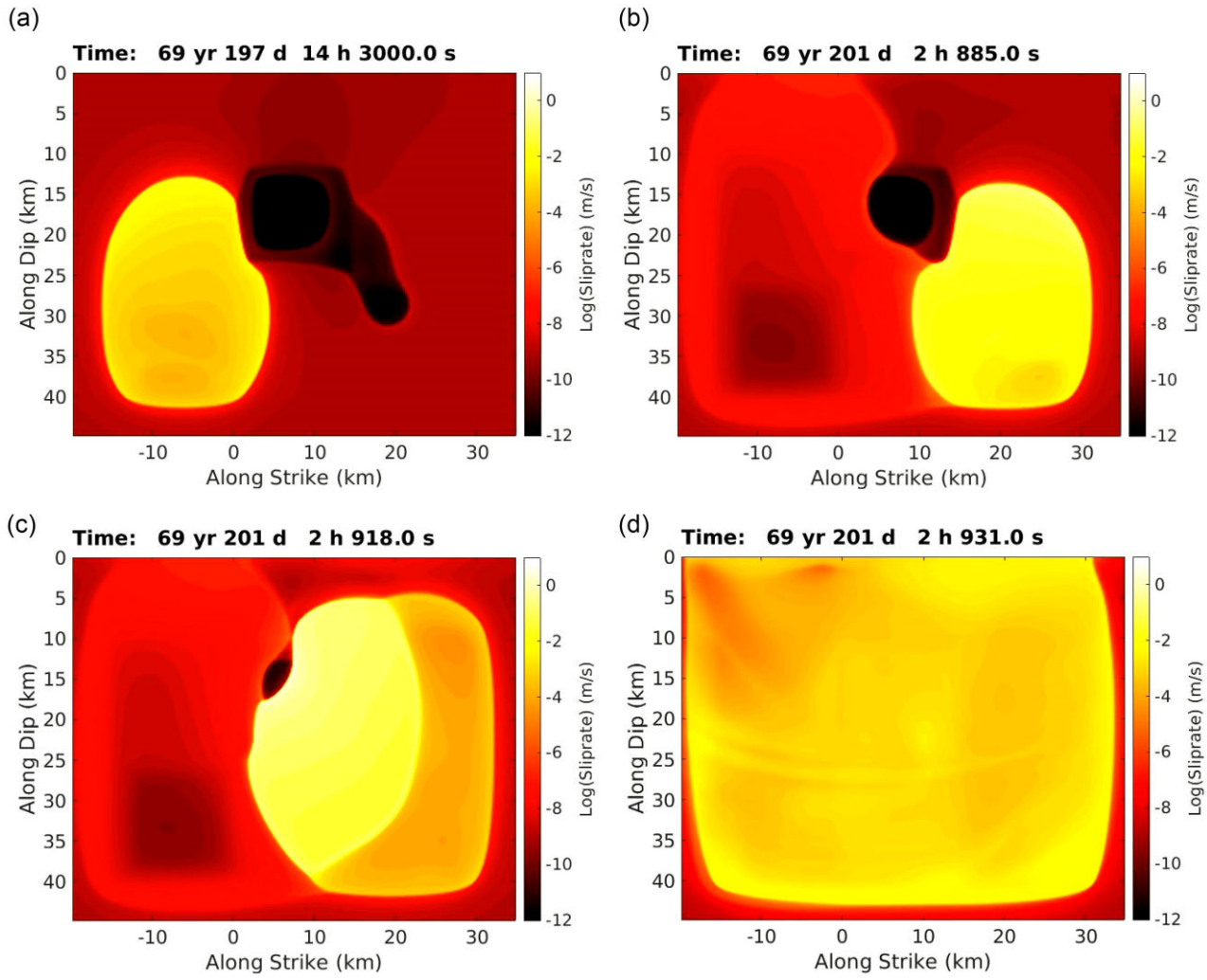

Figure 13. Snapshots of slip rate on the main fault during the dynamic event occurred at the 69th year, outlined by a dashed box in Fig. 12(e) for Model 6.

could also slow down rupture propagation and generate larger vertical seafloor displacement, contributing to tsunami generation (Ma 2012; Ma & Hirakawa 2013). Coffey *et al.* (2021) also proposed that coseismic slip on splay faults may actually produce large tsunami in the 1947 Poverty Bay (New Zealand) earthquakes. These factors may need to be taken into account and systematically compared in studying specific tsunami earthquakes or a specific subduction zone in the future. However, we limit this study to examine effects of subduction-interface frictional properties on tsunami earthquake characteristics in generic models.

Considering computational cost, we utilize an element size of 200 m (on the fault plane) in this study, which gives a ratio of the cohesive zone width over element size approximately 3 in the dynamic events from the models (Fig. S1). To verify that the results and conclusions from the 200 m element size models are robust, we conduct another simulation of Model 1 with a finer element size of 100 m (Figs S1 and S2). The slip/stress variations within the cohesive zone are well captured using the 200m element size, compared with those using the 100 m element size. In addition, we compare the rupture time contours of the first two dynamic events simulated using the 200 and 100 m element sizes (Fig. S2). The rupture time contours from the 200 m element size are close enough to those from the 100 m element size, suggesting the 200 m element size results are robust. We remark that our early studies (e.g. Duan & Day 2008) show that our finite element code EQdyna, on which the dynamic earthquake simulator is developed, can resolve the cohesive zone at a rupture front with about three elements, though four or more elements will be better. In addition, slow rupture propagation in tsunami earthquakes, which is the focus of this study, limits the Lorentz contraction effect from happening in our models. These may explain why we obtain good results with the 200 m element size.

6 CONCLUSIONS

This modelling study on tsunami earthquake generation advances our understanding of physics of tsunami earthquakes and demonstrates capability of a newly developed dynamic earthquake simulator in studying physics of subduction zone processes. The physics-based models in this study show that the conceptual model in which locally locked asperities are distributed in a conditionally stable shallow subduction interface works well in generating tsunami earthquakes. These asperities allow earthquakes to nucleate, and the conditionally stable friction environment surrounding the asperities gives rise to slow rupture propagation, long normalized duration and spectrum depleted in high frequency, characteristic features of tsunami earthquakes. The level of velocity-weakening

of the conditionally stable zone is critical to sustain rupture at slow speeds. High normal stress asperities, likely caused by subducted seamounts and other significant topographic highs, can act as barriers in some earthquakes while as asperities in other events in which large slip occurs on them. Their failures can propagate into wide areas of the conditionally stable zone and may trigger ruptures of other nearby asperities. Low normal stress asperities are relatively easy to be ruptured in a cascade fashion, generating a large tsunami earthquake with multiple seismic moment release pulses.

The dynamic earthquake simulator captures the dynamic rupture process of an earthquake cycle, in addition to other quasi-static processes that are typically the focus of traditional earthquake simulators. The capability allows us to examine spontaneous rupture propagation in the context of earthquake cycles, and thus to explore various slip behaviours (such as creep, slow-slip and earthquakes) and their interactions along subduction zones. Inclusion of the dynamic rupture process is critical to accurately capture dynamic interactions among locally locked asperities and thus final earthquake sizes. Because the dynamic simulator is based on an explicit finite element method, it does not need to solve systems of equations and thus has great potential to be further parallelized to make use of ever-increasing computing powers of modern high-performance computers. This needs collaboration between seismologists and computer scientists. We will work in this direction so that we can address scientific questions along large subduction zones worldwide.

ACKNOWLEDGEMENTS

This research is supported by NSF grants EAR-1254573, EAR-2013695, and Gangi/Heep professorship in theoretical geophysics from the College of Geosciences at Texas A&M University. The authors appreciate Texas A&M High Performance Research Computing (https://hprc.tamu.edu) for providing the advanced computer resources used in this study. This manuscript benefits greatly from constructive reviews provided by E. Dunham, two anonymous reviewers and Editor M. Segou. The authors also thank Dunyu Liu for helpful discussion during this study.

DATA AVAILABILITY

The data underlying this paper are available in the article, including the references cited.

REFERENCES

Abercrombie, R.E., Antolik, M., Felzer, K. & Ekström, G., 2001. The 1994 Java tsunami earthquake: slip over a subducting seamount, *J. geophys. Res.,* **106,** 6595–6607.

Ammon, C.J., Kanamori, H., Lay, T. & Velasco, A.A., 2006. The 17 July 2006 Java tsunami earthquake, *Geophys. Res. Lett.,* **33,** L24308, doi:10.1029/2006GL028005.

Andrews, D.J., 1976. Rupture velocity of plane strain shear cracks. *J. geophys. Res.,* **81**(32), 5679–5687.

Bassett, D., Sutherland, R. & Henrys, S., 2014. Slow wavespeeds and fluid overpressure in a region of shallow geodetic locking and slow slip, Hikurangi subduction margin, New Zealand. *Earth planet. Sci. Lett.,* **389,** 1–13.

Bell, R., Holden, C., Power, W., Wang, X. & Downes, G., 2014. Hikurangi margin tsunami earthquake generated by slow seismic rupture over a subducted seamount, *Earth planet. Sci. Lett.,* **397,** 1–9.

Ben-Zion, Y. & Rice, J. R., 1995. Slip patterns and earthquake populations along different classes of faults in elastic solids, *J. geophys. Res.,* **100**(B7), 12 959–12 983.

Bilek, S.L. & Lay, T., 2002. Tsunami earthquakes possibly widespread manifestations of frictional conditional stability, *Geophys. Res. Lett.,* **29,** 18-11–18-4.

Bilek, S.L. & Engdahl, E.R., 2007. Rupture characterization and aftershock relocations for the 1994 and 2006 tsunami earthquakes in the Java subduction zone, *Geophys. Res. Lett.,* **34,** L20311, doi:10.1029/2007GL031357.

Campus, P. & Das, S., 2000. Comparison of the rupture and radiation characteristics of intermediate and deep earthquakes, *J. geophys. Res.,* **105**(B3), 6177–6189.

Chen, T. & Lapusta, N., 2009. Scaling of small repeating earthquakes explained by interaction of seismic and aseismic slip in a rate and state fault model, *J. geophys. Res.,* **114**(B1), doi:10.1029/2008JB005749.

Courant, R., Friedrichs, K. & Lewy, H., 1967. On the partial difference equations of mathematical physics, *IBM J. Res. Dev.,* **11**(2), 215–234.

Coffey, G.L., Savage, H.M., Polissar, P.J., Meneghini, F., Ikari, M.J., Fagereng, Å., Morgan, J.K. & Wang, M., 2021. Evidence of seismic slip on a large splay fault in the Hikurangi subduction zone, *Geochem., Geophys., Geosyst.,* **22,** e2021GC009638.

Day, S.M., 1982. Three-dimensional finite difference simulation of fault dynamics: rectangular faults with fixed rupture velocity, *Bull. seism. Soc. Am.,* **72,** 705–727.

Day, S.M., Dalguer, L.A., Lapusta, N. & Liu, Y., 2005. Comparison of finite difference and boundary integral solutions to three-dimensional spontaneous rupture, *J. geophys. Res.,* **110**(B12), doi:10.1029/2005jb003813.

Dieterich, J.H., 1979. Modeling of rock friction: 1. Experimental results and constitutive equations, *J. geophys. Res.,* **84**(B5), 2161–2168.

Dieterich, J.H. & Richards-Dinger, K.B., 2010. Earthquake recurrence in simulated fault systems, *Pure appl. Geophys.,* **167,** 1087–1104.

Duan, B., 2010. Role of initial stress rotations in rupture dynamics and ground motion: a case study with implications for the Wenchuan earthquake, *J. geophys. Res.,* **115**(B5), doi:10.1029/2009JB006750.

Duan, B., 2012. Dynamic rupture of the 2011 Mw 9.0 Tohoku-Oki earthquake: roles of a possible subducting seamount, *J. geophys. Res.,* **117**(B5), doi:10.1029/2011JB009124.

Duan, B. & Day, S.M., 2008. Inelastic strain distribution and seismic radiation from rupture of a fault kink, *J. geophys. Res.,* **113**(B12), doi:10.1029/2008JB005847.

Duan, B. & Oglesby, D.D., 2006. Heterogeneous fault stresses from previous earthquakes and the effect on dynamics of parallel strike-slip faults, *J. geophys. Res.,* **111**(B5), doi:10.1029/2005JB004138.

Erickson, B.A. & Dunham, E.M., 2014. An efficient numerical method for earthquake cycles in heterogeneous media: alternating subbasin and surface-rupturing events on faults crossing a sedimentary basin, *J. geophys. Res.,* **119**(4), 3290–3316.

Harris, R.A. *et al.*, 2009. The SCEC/USGS dynamic earthquake rupture code verification exercise, *Seismol. Res. Lett.,* **80**(1), 119–126.

Harris, R.A. *et al.*, 2018. A suite of exercises for verifying dynamic earthquake rupture codes, *Seismol. Res. Lett.,* **89**(3), 1146–1162.

Houston, H., Benz, H.M. & Vidale, J.E., 1998. Time functions of deep earthquakes from broadband and short-period stacks, *J. geophys. Res.,* **103,** 29 895–29 913.

Hughes, T.J., 2000. *The Finite Element Method: Linear Static and Dynamic Finite Element Analysis,* Courier Corporation.

Ihmle´, P.F., 1996. Frequency-dependent relocation of the 1992 Nicaragua slow earthquake: an empirical Green's function approach, *Geophys. J. Int.,* **127,** 75–85.

Ihmle´, P.F., Gomez, J.M., Heinrich, P. & Guibourg, S., 1998. The 1996 Peru tsunamigenic earthquake: broadband source process, *Geophys. Res. Lett.,* **25,** 2691–2694.

Johnson, J.M. & Satake, K., 1997. Estimation of seismic moment and slip distribution of the April 1, 1946, Aleutian tsunami earthquake, *J. geophys. Res.,* **102,** 11765–11774.

Kanamori, H., 1972. Mechanism of tsunami earthquakes, *Phys. Earth planet. Inter.,* **6,** 346–359.

Kanamori, H. & Anderson, D.L., 1975. Theoretical basis of some empirical relations in seismology, *Bull. seism. Soc. Am.,* **65,** 1073–1095.

Kanamori, H. & Kikuchi, M., 1993. The 1992 Nicaragua earthquake: a slow tsunami earthquake associated with subducted sediments, *Nature,* **361,** 714–716.

Kaneko, Y., Ampuero, J.-P. & Lapusta, N., 2011. Spectral-element simulations of long-term fault slip: effect of low-rigidity layers on earthquake-cycle dynamics, *J. geophys. Res.,* **116**(B10), doi:10.1029/2011JB008395.

Kikuchi, M. & Kanamori, H., 1995. Source characteristics of the 1992 Nicaragua tsunami earthquake inferred from teleseismic body waves, *Pure appl. Geophys.,* **144**(3/4), 441–453.

Kimura, G., Hina, S., Hamada, Y., Kameda, J., Tsuji, T., Kinoshita, M. & Yamaguchi, A., 2012. Runaway slip to the trench due to rupture of highly pressurized megathrust beneath the middle trench slope: the tsunamigenesis of the 2011 Tohoku earthquake off the east coast of northern Japan, *Earth planet. Sci. Lett.,* **339-340,** 32–45.

Kitajima, H. & Saffer, D.M., 2012. Elevated pore pressure and anomalously low stress in regions of low frequency earthquakes along the Nankai Trough, *Geophys. Res. Lett.,* **39**(23),.

Lapusta, N. & Liu, Y., 2009. Three-dimensional boundary integral modeling of spontaneous earthquake sequences and aseismic slip, *J. geophys. Res.,* **114**(B9), doi:10.1029/2008JB005934.

Lapusta, N., Rice, J.R., Ben-Zion, Y. & Zheng, G., 2000. Elastodynamic analysis for slow tectonic loading with spontaneous rupture episodes on faults with rate-and state-dependent friction, *J. geophys. Res.,* **105**(B10), 23 765–23 789.

Lay, T., Ammon, C.J., Kanamori, H., Yamazaki, Y., Cheung, K.F. & Hutko, A.R., 2011. The 25 October 2010 Mentawai tsunami earthquake (Mw 7.8) and the tsunami hazard presented by shallow megathrust ruptures, *Geophys. Res. Lett.,* **38,** n/a, doi:10.1029/2010GL046552.

Liu, D. & Duan, B., 2018. Scenario earthquake and ground-motion simulations in north China: effects of heterogeneous fault stress and 3D basin structure, *Bull. seism. Soc. Am.,* **108,** 2148–2169.

Lotto, G.C., Dunham, E.M., Jeppson, T.N. & Tobin, H.J., 2017. The effect of compliant prisms on subduction zone earthquakes and tsunamis, *Earth planet. Sci. Lett.,* **458,** 213–222.

Lotto, G.C., Jeppson, T.N. & Dunham, E.M., 2018. Fully-coupled simulations of megathrust earthquakes and tsunamis in the Japan Trench, Nankai Trough, and Cascadia Subduction Zone, *Pure appl. Geophys.,* **176,** 4009–4041.

Luo, B. & Duan, B., 2018. Dynamics of non-planar thrust faults governed by various friction laws, *J. geophys. Res.,* **123,** 5147–5168.

Luo, B., Duan, B. & Liu, D., 2020. 3D finite-element modeling of dynamic rupture and aseismic slip over earthquake cycles on geometrically complex faults, *Bull. seism. Soc. Am.,* **110,** 2619–2637.

Ma, S. & Beroza, G.C., 2008. Rupture dynamics on a biomaterial interface for dipping faults, *Bull. seism. Soc. Am.,* **98**(4), 1642–1658.

Ma, S., 2012. A self-consistent mechanism for slow dynamic deformation and tsunami generation for earthquakes in the shallow subduction zone, *Geophys. Res. Lett.,* **39**(11), doi:10.1029/2012GL051854.

Ma, S. & Hirakawa, E.T., 2013. Dynamic wedge failure reveals anomalous energy radiation of shallow subduction earthquakes, *Earth planet. Sci. Lett.,* **375,** 113–122.

Ma, S. & Nie, S., 2019. Dynamic wedge failure and along-arc variations of tsunamigenesis in the Japan trench margin, *Geophys. Res. Lett.,* **46,** 8782–8790.

Masson, D.G., Parson, L.M., Milsom, J., Nichols, G., Sikumbang, N., Dwiyanto, B. & Kallagher, H., 1990. Subduction of seamounts at the Java trench—a view with long range sidescan sonar, *Tectonophysics,* **185**(1–2), 51–65.

Noda, H. & Lapusta, N., 2013. Stable creeping fault segments can become destructive as a result of dynamic weakening, *Nature,* **493**(7433), 518.

Pacheco, J.F., Sykes, L.R. & Scholz, C.H., 1993. Nature of seismic coupling along simple plate boundaries of the subduction type, *J. geophys. Res.,* **98**(B8), 14 133–14 159.

Pelayo, A.M. & Wiens, D.A., 1990. The November 20, 1960 Peru tsunami earthquake: source mechanism of a slow event, *Geophys. Res. Lett.,* **17,** 661–664.

Pelayo, A.M. & Wiens, D.A., 1992. Tsunami earthquakes: slow thrust-faulting events in the accretionary wedge, *J. geophys. Res.,* **97,** 15 321–15 337.

Pollitz, F.F., 2012. ViscoSim earthquake simulator, *Seismol. Res. Lett.,* **83**(6), 979–982.

Qiang, S., 1988. An adaptive dynamic relaxation method for nonlinear problems, *Comput. Struct.,* **30**(4), 855–859.

Rice, J.R., 1993. Spatio-temporal complexity of slip on a fault, *J. geophys. Res.,* **98**(B6), 9885–9907.

Rice, J. R. & Ben-Zion, Y., 1996. Slip complexity in earthquake fault models, *Proc. Natl. Acad. Sci.,* **93**(9), 3811–3818.

Rubin, A.M. & Ampuero, J.-P., 2005. Earthquake nucleation on (aging) rate and state faults, *J. geophys. Res.,* **110**(B11), doi:10.1029/2005jb003686.

Sallares, V. & Ranero, C.R., 2019. Upper-plate rigidity determines depth-varying rupture behaviour of megathrust earthquakes. *Nature,* **576**(7785), 96–101.

Sallares, V., Prada, M., Riquelme, S., Melendez, A., Calahorrano, A., Grevemeyer, I. & Ranero, C.R., 2021. Large slip, long duration, and moderate shaking of the Nicaragua 1992 tsunami earthquake caused by low near-trench rock rigidity, *Sci. Adv.,* **7**(32), doi:10.1126/sciadv.abg8659.

Sachs, M.K., Heien, E.M., Turcotte, D.L., Yikilmaz, M.B., Rundle, J.B. & Kellogg, L.H., 2012. Virtual California earthquake simulator, *Seismol. Res. Lett.,* **83**(6), 973–978.

Scholz, C.H., 1998. Earthquakes and friction laws, *Nature,* **391,** 37–42.

Scholz, C.H. & Small, C., 1997. The effect of seamount subduction on seismic coupling, *Geology,* **25,** 487–490.

Tanioka, Y. & Satake, K., 1996. Fault parameters of the 1896 Sanriku tsunami earthquake estimated from tsunami numerical modeling, *Geophys. Res. Lett.,* **23,** 1549–1552.

Tullis, T.E. *et al.*, 2012. Generic earthquake simulator, *Seismol. Res. Lett.,* **83**(6), 959–963.

Ward, S.N., 2012. ALLCAL earthquake simulator, *Seismol. Res. Lett.,* **83**(6), 964–972.

Yu, H., Liu, Y., Yang, H. & Ning, J., 2018. Modeling earthquake sequences along the Manila subduction zone: effects of three-dimensional fault geometry, *Tectonophysics,* **733,** 73–84.

SUPPORTING INFORMATION

Supplementary data are available at *GJI* online.

Figure S1. (a) Slip rate snapshot for one dynamic event in Model 1 simulated using grid size of 200m. (b) Slip and shear stress profiles at the same moment of the snapshot in (a) along a dashed line in strike direction. (c) Slip rate snapshot for a corresponding dynamic event in Model 1, while simulated using grid size of 100 m. (d) Slip and shear stress profiles at the same moment of the snapshot in (c) along a dashed line in strike direction.

Figure S2. Comparison of rupture time contours (where slip rate first arrives at 0.001 m s^{-1} on the fault plane) for the first dynamic event (a) and the second dynamic event (b) in Fig. 2(i) simulated by 200 m (black contours) and 100 m (red contours) grids.

Please note: Oxford University Press is not responsible for the content or functionality of any supporting materials supplied by the authors. Any queries (other than missing material) should be directed to the corresponding author for the paper.